HIGH ORDER LES FOR SUPERSONIC RAMP FLOW CONTROL WITH MVG

by

YONGHUA YAN

Presented to the Faculty of the Graduate School of

The University of Texas at Arlington in Partial Fulfillment

of the Requirements

for the Degree of

DOCTOR OF PHILOSOPHY

THE UNIVERSITY OF TEXAS AT ARLINGTON

May 2012

Copyright © by Yonghua Yan 2012

All Rights Reserved

ACKNOWLEDGEMENTS

Initially, I would like to thank my research advisor and committee chairman, Dr. Chaoqun Liu, for his guidance, advice, continuous support, encouragement, patience and understanding in both academics and life throughout my four years of study. It has been a true honor to work with him.

Also, I would like to thank the other committee members, Dr. Gaik Ambartsoumian, Dr. Guojun Liao, Dr. Hristo Kojouharov, and Dr. Yue Liu, for their understanding and support.

I would like to thank the Department of Mathematics, for the financial support during the long semesters through Graduate Teaching Assistantships, and I would also like to thank all colleagues for making my time at University of Texas at Arlington a great experience.

Finally, thanks to my wife, Caixia Chen, for her love, patience, understanding, kind support, encouragement, and for making this work interesting and a success. I am extremely fortunate to be so blessed. I am also extremely grateful to my family for their love and relentless support from overseas.

April 16, 2012

ABSTRACT

HIGH ORDER LES FOR SUPERSONIC RAMP

FLOW CONTROL WITH MVG

Yonghua Yan, PhD

The University of Texas at Arlington, 2012

Supervising Professor: Chaoqun Liu

An implicitly implemented large eddy simulation by using the fifth order bandwidth-optimized WENO scheme is applied to make comprehensive studies on ramp flows with and without control at Mach 2.5 and Re_θ=5760. Flow control in the form of microramp vortex generators (MVG) is applied. The results show that MVG can distinctly reduce the separation zone at the ramp corner and lower the boundary layer shape factor under the condition of the computation.

A series of new findings are obtained about the MVG-ramp flow including the three-dimensional vortex structure generated by MVG. The mechanism about the formation vortex ring structure and its interaction with shock wave at the ramp corner is deeply studied. Vortex rings strongly interact with the flow and play an important role in the separation zone reduction. It shows that the ring structure does not break down and keeps it topology after penetrating the strong shock wave and the oblique shocks is influenced a lot by the induced flow field from rings. The bump of the 3D shock wave surface is discovered and its mechanism is explained.

TABLE OF CONTENTS

ACKNOWLEDGEMENTS ..... ……..iii

ABSTRACT.....iv

LIST OF ILLUSTRATIONS.....vii

LIST OF TABLES.....xi

Chapter Page

1. INTRODUCTION……..……..…..... .1

2. NAVIER-STOKES EQUATIONS 6

2.1 Conservation Laws and the Equations..... 6

2.2 Non-Dimensional Form..... 7

2.3 Expansion in Curvilinear Coordinates 8

3. NUMERICAL METHODS FOR SUPERSONIC RAMP FLOW..... 12

3.1 Numerical Scheme 12

3.1.1 The 5th Order Bandwidth-optimized WENO Scheme for the Convective Terms 12

3.1.2 The Difference Scheme for the Viscous Terms..... 16

3.1.3 The Time Scheme 16

3.2 Grid Generation..... 16

3.3 Boundary Conditions 22

3.4 Code Validation..... 24

4. NUMERICAL RESULTS FOR SUPERSONIC RAMP FLOW 28

4.1 Inflow Boundary Layer Profiles 28

4.2 Results of the Supersonic Ramp Flow(without MVG)..... 29

4.2.1 Flow Structures of the Instantaneous and Averaged Flow..... 29

4.2.2 The Length of the Separation Zone by SBLI 31

4.2.3 The Quality of the Downstream Boundary Layer After the Separating Corner 32

4.3 Results of the MVG Controlled Ramp Flow 32

4.3.1 Velocity Profile Behind MVG 32

4.3.2 The Three Dimensional Shock/Expansion Wave System of the MVG-ramp Flow 33

4.3.3 The Topology of the Separation and Vortices of the MVG Flow 36

4.3.4 The Formation of the Streamwise Momentum Deficit After the MVG 43

4.3.5 Vortex Rings - A New Mechanism in MVG-ramp Flow Control 46

4.3.6 The Characteristics of the Separation and the Comparison with the Ramp Flow without MVG 49

4.3.7 The Quality of the Downstream Boundary Layer and the Effect of the Control 50

5. NUMERICAL STUDY ON THE MECHANISM OF VORTEX RINGS 52

5.1 Vortex Ring Structure 52

5.2 Conservation of Vorticity 58

5.3 Stability Analysis to the Velocity Profile 61

5.3.1 Derivation of Linear Stability Equation 63

5.3.2 Stability Analysis to the Averaged Velocity Profile 64

6. NUMERICAL STUDY ON SHOCK WAVE-VORTEX RING INTERACTION 68

6.1 Influence on Ring Structure by the Interaction 68

6.2 Influence on Oblique Shock Wave 74

7. CONCLUDING REMARKS 80

REFERENCES 82

BIOGRAPHICAL INFORMATION 88

LIST OF ILLUSTRATIONS

Figure Page

3.1 Grid Stencils for 5th Order WENO 12

3.2 Grid Stencils for 5th Order Bandwidth-optimized WENO 14

3.3 The Geometry of MVG. 17

3.4 The Schematic of the Half Grid System of Case 1. 18

3.5 The Geometry Sketch of the Ramp..... 18

3.6 The Grid System of Case 1. 19

3.7 The Local View of Grids around the Trailing-edge..... 19

3.8 The Surface Grids of MVG in Patches. 19

3.9 The Grids in Certain Cross-section. 20

3.10 The Grids at the Foot of the Trailing-edge..... 21

3.11 The Grids at the Ramp Corner..... 21

3.12 The Contour of the Pressure..... 24

3.13 The Comparison of the Pressure. 24

3.14 The Comparison of the Shock Location with that of Rusunov. 25

3.15 The Converging History of the 5th WENO Scheme. 25

3.16 The Pressure Contour at the Central Plane and Body Surface. 26

3.17 The Spatial Streamlines. 26

3.18 (a) The Instantaneous Digital Schlieren at Central Plane
(ramp angle is 24 degree) and (b) The Schlieren Pictures from
the Experiment (ramp angle is 25 degree). 27

3.19 (a) The Schlieren Picture from Babinsky and
(b) The Numerical Schlieren Picture at the Central Plane. 27

4.1 Inflow Boundary-layer Profile Comparison with GUARINI et al's
(a) Inflow Velocity Profile by Our Computation and

(b) Inflow Velocity Profile by Guarini [54] ($U^{**} = 2.5\log y^{+} + 4.7$). 29

4.2 The Pressure Contour at the Central Plane and Body Surface. 30

4.3 The Cross-section Streamlines at the Central Plane. 30

4.4 Qualitative Comparison of Averaged Velocity Profile behind MVG with Experiment
(a) Averaged Velocity Profile behind MVG
(b) Averaged Velocity Profile by Babinsky et al. 33

4.5 The Overview of the 3-D Structure of the Shock Waves. 35

4.6 The 3-D Structure at the Inter-mediate Section 1 (a) and 2 (b). 35

4.7 The Time-averaged (upper) and Instantaneous (lower) Surface Pressure. 36

4.8 The Surface Oil Flow by Babinsky. 37

4.9 The Surface Limiting Streamlines by Computation. 37

4.10 The Separation Pattern near the end of MVG. 38

4.11 The Various Views of Surface Separation Pattern (SSP)
(a) SSP on the Side of MVG
(b) SSP Backgrounded Using the Pressure Contour. 38

4.12 The Dynamic Vortex Model. 39

4.13 The Comparison between the Computation and the Validating Experiment. 39

4.14 The Locations of the Cross Sections
($L_{from\ apex}/h \approx 1.15$, 3.04, 6.45, 14.95, 18.78 and 27.41). 41

4.15 The Streamlines at Cross Section 2. 42

4.16 The Streamlines at Cross Section 3. 42

4.17 The Streamlines at Cross Section 4. 42

4.18 The Streamlines at Cross Section 5. 42

4.19 The Streamlines at Cross Section 6. 43

4.20 The Contour of the Averaged Streamwise Velocity at Section 2. 44

4.21 The Spatial Stream-lines passing through the Boundary of Deficit. 44

4.22 The Cross-section Streamlines. 44

4.23 The Streamwise Velocity Contour at two Streamwise Computational Planes. 45

4.24 The Streamwise Velocity Contour at a Horizontal Computational Plane. 45

4.25 The Iso-surface of the Streamwise Velocity. 45

4.26 The Instantaneous Spatial Streamlines. 47

4.27 The Iso-surface of the Instantaneous Pressure. 47

4.28 Vortex Rings shown by the Iso-surface of λ_2. 48

4.29 The Side View of Vortex Rings on the Ramp. 49

4.30 Surface Limiting Streamlines at SBLI Region. 49

4.31 The Time-averaged (left) and Instantaneous (right)
Friction Coefficient Distribution at SBLI Region. 49

4.32 The Distribution of the Time-averaged Streamwise Velocity of the two Cases. 50

4.33 Comparison of the Mean Wall Pressure Distribution at the Centerline
after the MVG (both on the base plate and the ramp surface). 51

5.1 The Numerical Shilieren at the Center Plane. 52

5.2 The Laser-sheet Flash Image at the Center Plane (Lu et al 2010).
(a) Using PIV, (b) Using the Acetone Vapor. 53

5.3 K-H Rings behind MVG by (Sun et al 2011). 53

5.4 Distribution of Kelvin-Helmholtz Vortices and Streamwise Vortices from LES. 54

5.5 Vortex Rings shown by the Components of Vorticity
(a) Global View (b) Close-up View. 54

5.6 Part of the Ring Structure shown by Total Vorticity Magnitude (left)
and each Components (right). 55

5.7 Part of the Ring Structure shown by λ_2(from the bottom view). 56

5.8 The Velocity Field on the Cross Section. 57

5.9 The Velocity Field close to the Foot (left) and the Head (right) of a Vortex Ring. 57

5.10 The Scope for Vorticity Magnitude Check. 58

5.11 The Instantaneous Vorticity Distribution. 59

5.12 Averaged Streamwise Velocity at Different Sections. 61

5.13 Inflection Points (surface for 3-D)
(a) Averaged Streamwise Velocity at $L_{from\ apex}/h \approx 3.3$ (b) $\partial^2 w/\partial y^2$. 62

5.14 Eigenvector Function of $\hat{v}$. 66

5.15 The Instantaneous Vorticity Distribution. 67

6.1 The Three Vortex Rings above the Ramp for Measurement. 69

6.2 The 3D View of the Propagating Rings at the Ramp part at Different Time. 70

6.3 The Ring Structure at the Ramp part by λ_2. 71

6.4 Streamwise Vorticity Distribution at two Different Time Steps. 71

6.5 Iso-surface of $|\nabla\rho\times\nabla p|$ in the Ramp Part.
(a) $|\nabla\rho\times\nabla p|=80$ (b) $|\nabla\rho\times\nabla p|=40$ (c) $|\nabla\rho\times\nabla p|=20$ (d) $|\nabla\rho\times\nabla p|=10$ 73

6.6 Density Gradients (left) and Pressure Gradient (right) on the Central Plane. 74

6.7 Contours of a) $|\nabla\rho|$ and (b) $|\nabla p|$ at Two Moments at the Center Planes. 75

6.8 The Contours of (a) $|\nabla\rho|$ and (b) $|\nabla p|$ at Spanwise Sections
and at Four Successive Moments. 75

6.9 The Shock Wave Shape by the Iso-surface of Pressure and Ring Structure by λ_2. 76

6.10 The 3D Shock Wave Shape by $|\nabla p|$. 77

6.11 The Vector Field at a Spanwise Section with
Vortex Structure shown by Total Vorticity. 79

LIST OF TABLES

Table Page

3.1 The Geometric Parameters for the Computation 21

6.1 Characteristic Parameters of Vortex Rings on the Plate 69

CHAPTER 1

INTRODUCTION

Micro vortex generators (VG) are a kind of low-profile passive control device designed for the boundary layer control. In contrast to the conventional VG (widely used in aviation applications and with height (h) of the order of the boundary-layer (δ)), micro VG has a height approximately 20-40% (more or less) of the boundary layer. As we know, in the supersonic ramp flows, shock boundary layer interaction (SBLI) can significantly reduce the quality of the flow field by triggering large-scale separation, causing total pressure loss, and making the flow unsteady and distorting. The consequences of the interaction often degrade the performance of the engine and even make an engine unable to start. Micro VG is a new device which is designed to alleviate or overcome such difficulties and, therefore, to improve the “health” of the boundary layer. There are more than one kind of micro VG, like the micro vane and micro ramp VG (MVG). Because MVG has a more robust structure, it becomes more attractive to the inlet designer. Intensive computational and experimental studies have been made on it recently.

In Lin’s review [1] on the low-profile vortex generator, it was mentioned that a device like MVG could alleviate the flow distortion in compact ducts to some extent and control boundary layer separation due to the adverse pressure gradients. Similar comments were made in the review by Ashill et al [2]. The formal and systematic studies about the micro VGs including micro ramp VG can be found in the paper of Anderson et al [3]. Micro-actuators including MVG were found to have comparable effects as the boundary layer bleeding technique, and so MVG was considered to be very practical for the flow control in supersonic inlets. A series of experimental and computational investigations have been carried out since then. The most prominent experimental studies reported are those by Babinsky [4-7]. He made a series of experiments on different kinds of mirco VGs and investigated their control effects in

detail. The mechanism of MVG flow control from his work concludes that a pair of counter-rotating primary streamwise vortices is generated by MVG, which are mainly located within the boundary layer and travel downstream for a considerable distance. Secondary vortices are located underneath the primary ones and even more streamwsie vortices could be generated under suitable conditions. Streamwise vortices inside the boundary later bring low momentum fluid up from the bottom and high momentum fluid down to the boundary layer. A striking circular momentum deficit region is observed in the wake behind the MVG. The vortices keep lifting up slowly, which is thought to be the consequence of the upwash effect of the vortices.

Numerical simulations have been made on MVG for comparative study and further design purposes. Ghosh, Choi and Edwards [8] made detailed computations under the experimental conditions given by Babinsky. These numerical studies include RANS computations and hybrid RANS/LES computations using immersed boundary (IB) techniques. The fundamental structures, like the streamwise vortices and momentum deficit, were reproduced by the computation. Lee et al [9] also made computations on the micro VGs problems by using Monotone Integrated Large Eddy Simulations (MILES). In their computation, the MVG is placed in a domain with the configuration following the real wind tunnel. The fundamental wave system of the MVG were reproduced in the computation, which consists of the main shock, expansion waves and re-compression shock like that reported by Babinsky [6]. The momentum deficit was captured too. They [10] further tested several variations of the standard MVG and micro vane to enhance the control effect.

As we know, the purpose of the MVG is to control the shock induced separation and to improve the quality of the boundary layer velocity profile after the SBLI. Supersonic ramp flow is a typical prototype SBLI problem, and the ramp configuration often exists in the engine and control surfaces in high speed vehicles. The fundamental problem of the ramp flow includes the determination of characteristics and criteria of the flow separation and reattachment, the mechanism of the shock unsteadiness and the aerodynamic/thermal correspondence, etc.

Many experimental studies had been made on these problems. Some well recognized ones can be found from the work by Dolling [11-13], Settles [14], Dussauge [15], Andreopoulos [16], Loginov [17] and their collaborators. For numerical simulations, there are three basic categories, i.e., the RANS, LES and DNS. It is well-known that RANS models do not perform well for SWTBLI (Wilcox [18], 1993). According to Zheltovodov's opinion [19], the existing RANS models cannot solve the strong SBLI problem accurately, including the supersonic ramp flow. About the numerical works of LES, Rizzetta and Visbal [20] made simulations on a compression corner by implicit LES using a high-order method; Kaenal, Kleiser, Adams, and Loginov et al conducted LES [21] on ramp flow using an approximate de-convolution model developed by Stolz. The comparisons were made and some agreement was obtained between the computational and the available experimental results. The first DNS on supersonic ramp flow was made by Adams for a 10° compression ramp at Mach 3 and Re_θ=1685. In the work done by Adams [22] and his colleagues, the 5th order hybrid compact-ENO scheme was applied. Later Martin and the collaborators made a series of remarkable investigations by using DNS [23-28]. Comparisons were made between the computation and the experiments from the low Reynolds number wind tunnel at Princeton University [29]. They used the fifth order bandwidth-optimized WENO scheme which is the same scheme that the current work uses. The effect of low Reynolds number on the separation was studied. More work on MVG and other flow control tools have been done recently [30-35]. According to the experimental and numerical research, some flow mechanisms are recognized as: a) the amplification of the turbulence after the SBLI is thought to be caused by the nonlinear interaction between the shock wave and the coupling of turbulence, vorticity and entropy waves [36]; b) the unsteady motion of the shock is considered to be generated by the very long low-momentum coherent structures in logarithmic layer and such structures might be formed by the hairpin vortex packet.

Although there are experiments and computations on MVG and ramp problems, these investigations were carried out separately. The combination of MVG and ramp is not conducted

yet and it is unclear if the MVG can be used to control the supersonic ramp flow. In order to carry out flow control more effectively using MVG, the mechanism of the flow should be carefully studied first. There are at least three problems which should be clarified: a) what is the three-dimensional structures of the wave system caused by MVG. Till now, only two-dimensional structural information was available and confirmed by experiment; b) what is the relation between the momentum deficit and the flow structure and where does the low speed fluid come from? c) Is there any new mechanism besides the pronounced momentum transportation and mixing by streamwise vortices?

In this study, we investigate the control effect of MVG on the supersonic ramp flow with a fully developed turbulent inflow by numerical simulations, and further explore the mechanisms related to those questions mentioned above. Numerical simulations are made on supersonic ramp flow with and without MVG control at Mach 2.5 and Re_θ=5760. The trailing edge declining angle of the MVG is 70° in computation. In order to make simulations, a kind of large eddy simulation method is used by solving the unfiltered form of the Navier-Stokes equations (NSEs) with the 5th order bandwidth-optimized WENO scheme, which is generally referred to the so-called implicitly implemented LES. Without explicitly using the subgrid scale (SGS) model as the explicit LES, the implicitly implemented LES uses the intrinsic dissipation of the numerical method to dissipate the turbulent energy accumulated at the unresolved scales with high wave numbers. There are two main subfields about this category, i.e., the MILES [39-40] by Boris, Fureby and Grinstein, et al, and the implicit LES [41, 42] by Visbal, Rizzetta and Gaitonde, et al. The first subfield is based on modified equation analysis, and typically uses the high order monotone scheme like flux-corrected transport (FCT) scheme or piecewise parabolic method (PPM). The *ENO* algorithm was also reported being used as the limiter in Ref. 41. This kind of method can be used to solve the supersonic problems with shock waves, but the order of the scheme should not be competitive to the modern high order schemes like the compact schemes or *WENO* schemes with 5th order of accuracy or higher. The second one [42] specifically uses

the high order compact scheme by Lele and the high order Pade-type low-pass spatial filter. However, the published applications of the method are only for the low speed flow. When the same numerical algorithms were used on supersonic problems [43-44], the Smagorinsky dynamic SGS model was incorporated in the simulation, which implies the existence of issues related to the numerical stability. A series of shock-capturing schemes were also tried for large eddy simulation [45-46], including the WENO scheme. As mentioned in Ref. 46, at low Mach number the investigated compact differencing and filter scheme formulation may give better results but as the Mach number increases the relative suitability of the ENO method increases. However, the ENO scheme still produces numerical turbulence thus stabilizing filters is need, while the WENO scheme does not need filtering. Recently, an evaluating computation was reported on circular cylinder flow using implicitly implemented LES by the 5th WENO scheme [47]. Comparisons were made between the computation and the experiment. The results show that the numerical algorithm is feasible and efficient. For the studied supersonic MVG controlled ramp flow problem, there are complex shock wave system, strong shock-vortex interaction and small scale structures. Considering the above status of implicitly implemented LES, the method by solving the NSEs with the 5th order bandwidth-optimized WENO scheme is used in the paper and considered as certain implicitly implemented LES.

The structure of the dissertation is as follows. In Chapter 2, the Navier-Stokes equations are introduced. In Chapter 3, the numerical scheme, the grid information and the boundary conditions are discussed. In Chapter 4, the computational results of supersonic ramp flow with and without MVG are presented; a series of new findings including the vortex ring structure generated by MVG is stated. In Chapter 5, the mechanism of vortex ring generation is analyzed in detail. Finally, in Chapter 6, a study on shock wave-vortex ring Interaction is made.

CHAPTER 2

NAVIER-STOKES EQUATIONS

2.1 Conservation Laws and the Equations

The motion of a fluid can be described by the conservation of mass, momentum, and of energy for an arbitrary small control volume.

Consider a closed surface S whose position is fixed with relation to the coordinate axes and encloses a volume V completely filled with fluid. Given the density of the fluid ρ, the momentum $\rho\boldsymbol{u}$, the total energy E at a position $\boldsymbol{x}$ and at time t, the Navier-Stokes equations can be derived as follows from the conservation laws of mass, momentum and energy:

$$\frac{\partial \rho}{\partial t} + \nabla \cdot (\rho \boldsymbol{u}) = 0 \tag{2.1}$$

$$\frac{\partial (\rho \boldsymbol{u})}{\partial t} + \nabla \cdot (\rho \boldsymbol{u} \otimes \boldsymbol{u}) = (\nabla \cdot \sigma) \tag{2.2}$$

$$\frac{\partial (\rho E)}{\partial t} + \nabla \cdot (\rho E)\boldsymbol{u} - \nabla \cdot (k \nabla T) - \nabla \cdot (\sigma \cdot \boldsymbol{u}) = 0 \tag{2.3}$$

With

$$E = e + \frac{\boldsymbol{u} \cdot \boldsymbol{u}}{2} \tag{2.4}$$

and

$$\sigma = -\left[p + \frac{2}{3}\mu(\nabla \cdot \boldsymbol{u}) \right] \boldsymbol{I} + \mu\left[\nabla \boldsymbol{u} + (\nabla \boldsymbol{u})^T \right] \tag{2.5}$$

Here, σ is the internal shear stress, e is the internal energy per unit mass of the fluid, p denotes the pressure, T represents the temperature, k is the thermal conductivity and μ is the

dynamic viscosity. Stokes(1845) assumption (linear relation between the stress and the rate of strain of the fluid) is used in obtaining the equation (2.5).

In three dimensions, the system above contains five equations (the conservation of momentum equation becomes three separate equations). Two extra equations are needed to solve the system for the unknown variables ρ, $\boldsymbol{u}$, p, E, and T. These equations are the equation of state, for a thermally perfect gas,

$$p = \rho RT \tag{2.6}$$

where R is a gas constant, and the equation for internal energy equation,

$$e = c_v T \tag{2.7}$$

2.2 Non-Dimensional Form

Equations (2.1)-(2.6) can be reduced to a non-dimensional form. This can be achieved by dividing each variable by an appropriate dimensional reference parameter. Those reference parameters are defined as follows, where ∞ indicates incoming or free stream values:

L is the characteristic length;

V_∞ is the speed;

ρ_∞ is the density;

p_∞ is the pressure;

T_∞ is the temperature;

μ_∞ is the dynamic viscosity;

k_∞ is the thermal conductivity.

With these reference parameters, the non-dimensional variables are given by

$$t = \frac{t^*}{L/V_\infty},\ \boldsymbol{x} = \frac{\boldsymbol{x}^*}{L},\ \boldsymbol{u} = \frac{\boldsymbol{u}^*}{V_\infty},\ p = \frac{p^*}{\rho_\infty V_\infty^2},\ \boldsymbol{\sigma} = \frac{\boldsymbol{\sigma}^*}{\rho_\infty V_\infty^2} \tag{2.8}$$

where * represents the dimensional variables.

We can rewrite the equations of section 2.1 in non-dimensional form, obtaining:

$$\frac{\partial \rho}{\partial t} + \nabla \cdot (\rho \boldsymbol{u}) = 0 \tag{2.9}$$

$$\frac{\partial (\rho \boldsymbol{u})}{\partial t} + [\nabla \cdot (\rho \boldsymbol{u} \otimes \boldsymbol{u})] = (\nabla \cdot \sigma) \tag{2.10}$$

$$\frac{\partial (\rho E)}{\partial t} + \nabla \cdot (\rho E)\mathbf{u} - \frac{\gamma}{RePr} \nabla \cdot (\nabla T) - \gamma(\gamma - 1) M_\infty^2 \nabla \cdot (\sigma \cdot \mathbf{u}) = 0 \tag{2.11}$$

$$\sigma = -\left[p + \frac{2}{3} \frac{1}{Re} \mu(T)(\nabla \cdot \boldsymbol{u}) \right] \boldsymbol{I} + \frac{1}{Re} \mu(T) \left[\nabla \boldsymbol{u} + (\nabla \boldsymbol{u})^T \right] \tag{2.12}$$

$$p = \frac{1}{\gamma M_\infty^2} \rho T \tag{2.13}$$

The Reynolds number is defined as

$$Re = \frac{\rho_\infty V_\infty L}{\mu_\infty} \tag{2.14}$$

while the Prandtl number evaluated at the reference conditions is given by

$$Pr = \frac{c_p \mu_\infty}{k_\infty} \approx 0.72 \tag{2.15}$$

and the Mach number is defined as

$$M_\infty = \frac{V_\infty}{\sqrt{\gamma R T_\infty}} \tag{2.16}$$

The dynamic viscosities coefficient is given by Sutherland's equation:

$$\mu = T^{\frac{3}{2}} \frac{1 + C}{T + C}, \; C = \frac{110.4}{T_\infty} \tag{2.17}$$

2.3 Expansion in Curvilinear Coordinates

In vector form, we may rewrite the equations as

$$\frac{\partial Q}{\partial t}+\frac{\partial E}{\partial x}+\frac{\partial F}{\partial y}+\frac{\partial G}{\partial z}=\frac{\partial E_v}{\partial x}+\frac{\partial F_v}{\partial y}+\frac{\partial G_v}{\partial z} \tag{2.18}$$

where

$$Q=\begin{bmatrix}\rho\\ \rho u\\ \rho v\\ \rho w\\ e\end{bmatrix}\quad E=\begin{bmatrix}\rho u\\ \rho u^2+p\\ \rho uv\\ \rho uw\\ (e+p)u\end{bmatrix}\quad F=\begin{bmatrix}\rho v\\ \rho vu\\ \rho v^2+p\\ \rho vw\\ (e+p)v\end{bmatrix}\quad G=\begin{bmatrix}\rho w\\ \rho wu\\ \rho wv\\ \rho w^2+p\\ (e+p)w\end{bmatrix} \tag{2.19}$$

$$E_v=\frac{1}{\mathrm{Re}}\begin{bmatrix}0\\ \tau_{xx}\\ \tau_{xy}\\ \tau_{xz}\\ u\tau_{xx}+v\tau_{xy}+w\tau_{xz}+q_x\end{bmatrix} \tag{2.20}$$

$$F_v=\frac{1}{\mathrm{Re}}\begin{bmatrix}0\\ \tau_{yx}\\ \tau_{yy}\\ \tau_{yz}\\ u\tau_{yx}+v\tau_{yy}+w\tau_{yz}+q_y\end{bmatrix} \tag{2.21}$$

$$G_v=\frac{1}{\mathrm{Re}}\begin{bmatrix}0\\ \tau_{zx}\\ \tau_{zy}\\ \tau_{zz}\\ u\tau_{zx}+v\tau_{zy}+w\tau_{zz}+q_z\end{bmatrix} \tag{2.22}$$

$$q_x=\frac{\mu}{(\gamma-1){M_\infty}^2\,\mathrm{Pr}}\frac{\partial T}{\partial x},\ q_y=\frac{\mu}{(\gamma-1){M_\infty}^2\,\mathrm{Pr}}\frac{\partial T}{\partial y},\ q_x=\frac{\mu}{(\gamma-1){M_\infty}^2\,\mathrm{Pr}}\frac{\partial T}{\partial z} \tag{2.23}$$

$$p = \frac{1}{\gamma M_\infty^2} \rho T \tag{2.24}$$

$$\tau = \mu \begin{bmatrix} \frac{4}{3}\frac{\partial u}{\partial x} - \frac{2}{3}(\frac{\partial v}{\partial y} + \frac{\partial w}{\partial z}) & \frac{\partial u}{\partial y} + \frac{\partial v}{\partial x} & \frac{\partial u}{\partial z} + \frac{\partial w}{\partial x} \\ \frac{\partial u}{\partial y} + \frac{\partial v}{\partial x} & \frac{4}{3}\frac{\partial v}{\partial y} - \frac{2}{3}(\frac{\partial w}{\partial z} + \frac{\partial u}{\partial x}) & \frac{\partial v}{\partial z} + \frac{\partial w}{\partial y} \\ \frac{\partial u}{\partial z} + \frac{\partial w}{\partial x} & \frac{\partial v}{\partial z} + \frac{\partial w}{\partial y} & \frac{4}{3}\frac{\partial w}{\partial z} - \frac{2}{3}(\frac{\partial u}{\partial x} + \frac{\partial v}{\partial y}) \end{bmatrix} \tag{2.25}$$

Let us assume that the position frame of reference is fixed in time, that is, the generalized coordinates do not change with time. Then, we can define the curvilinear coordinates in relation to the Cartesian coordinates as

$$\begin{cases} \xi = \xi(x, y, z) \\ \eta = \eta(x, y, z) \\ \zeta = \zeta(x, y, z) \end{cases} \tag{2.26}$$

The Navier-Stokes equations can be transformed to the system using generalized coordinates:

$$\frac{\partial \hat{Q}}{\partial \tau} + \frac{\partial \hat{E}}{\partial \xi} + \frac{\partial \hat{F}}{\partial \eta} + \frac{\partial \hat{G}}{\partial \zeta} = \frac{\partial \hat{E}_v}{\partial \xi} + \frac{\partial \hat{F}_v}{\partial \eta} + \frac{\partial \hat{G}_v}{\partial \zeta} \tag{2.27}$$

Where $\hat{Q} = J^{-1} Q$ and

$$\hat{E} = J^{-1}(\xi_x E + \xi_y F + \xi_z G) \tag{2.28}$$

$$\hat{F} = J^{-1}(\eta_x E + \eta_y F + \eta_z G) \tag{2.29}$$

$$\hat{G} = J^{-1}(\zeta_x E + \zeta_y F + \zeta_z G) \tag{2.30}$$

$$\hat{E}_v = J^{-1}(\xi_x E_v + \xi_y F_v + \xi_z G_v) \tag{2.31}$$

$$\hat{F}_v = J^{-1}(\eta_x E_v + \eta_y F_v + \eta_z G_v) \tag{2.32}$$

$$\hat{G}_v = J^{-1}(\zeta_x E_v + \zeta_y F_v + \zeta_z G_v) \tag{2.33}$$

$$J^{-1} = \det\left(\frac{\partial(x, y, z)}{\partial(\xi, \eta, \zeta)}\right) \tag{2.34}$$

CHAPTER 3

NUMERICAL METHODS FOR SUPERSONIC RAMP FLOW

3.1 Numerical Scheme

3.1.1. The 5th Order Bandwidth-optimized WENO Scheme for the Convective Terms

For integrity, the 5th order WENO will be described as follows. Considering the one dimensional hyperbolic equation,

$$\frac{\partial u}{\partial t} + \frac{\partial f(u)}{\partial x} = 0 \tag{3.1}$$

The semi-discretized equation by the conservative scheme can be expressed as,

$$\left(\frac{\partial u}{\partial t}\right)_j = -\frac{h_{j+1/2} - h_{j-1/2}}{\Delta x} \tag{3.2}$$

where $h_{j+1/2} = h\left(f_{j+1/2}\right)$ and for second order scheme, $h_{j+1/2} = f_{j+1/2}$.

The basic ideas of the weighted schemes like WENO are as follows,

(1) Apply basic grid stencils and difference schemes on them

(2) Combine these schemes on different stencils and get linear weights to obtain higher order

(3) Obtain nonlinear weights to make the scheme adaptive to discontinuity like shock waves.

Fig. 3.1 shows the basic grid stencils for standard 5th order WENO scheme [48]

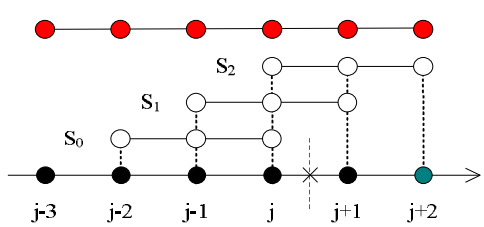

Figure 3.1 Grid Stencils for 5th Order WENO

Considering the positive flux, the three upwind-biased schemes on three candidates can be given as,

$$\begin{cases} h^{+\prime}{}_1 = \frac{1}{3} f_{j-2} - \frac{7}{6} f_{j-1} + \frac{11}{6} f_j \\ h^{+\prime}{}_2 = -\frac{1}{6} f_{j-1} + \frac{1}{3} f_j + \frac{5}{6} f_{j+1} \\ h^{+\prime}{}_3 = \frac{1}{3} f_j + \frac{5}{6} f_{j+1} - \frac{1}{6} f_{j+2} \end{cases} \tag{3.3}$$

The mark '+' refers to the positive flux after flux splitting. 3rd order is obtained for each individual scheme. Schemes on basic stencils are symmetric to the one with respect to $x_{j+1/2}$. Weighting and the linear weights to obtain higher order:

$$h^{+}{}_{Linear,\, j+1/2} = \alpha_1 h^{+\prime}{}_1 + \alpha_2 h^{+\prime}{}_2 + \alpha_3 h^{+\prime}{}_3 \tag{3.4}$$

The optimal order for the weighted scheme is 2*r*+1, where *r* is the number of the stencil. The order of the scheme is 5th order. When the optimal order is realized, the α_i must be determined as:

$$(\alpha_1, \alpha_2, \alpha_3) = (0.1, 0.6, 0.3) \tag{3.5}$$

The nonlinear weighted schemes can be expressed as:

$$h^{+}{}_{j+1/2} = w_1 h^{+\prime}{}_1 + w_2 h^{+\prime}{}_2 + w_3 h^{+\prime}{}_3 \tag{3.6}$$

where w_i is changing from place to place, and

$$w_i = b_i / (b_1 + b_2 + b_3) \tag{3.7}$$

$$b_i = \alpha_i / (\varepsilon + IS_i)^2 \tag{3.8}$$

and ε is a small quantity to prevent the denominator from being zero, which should be small enough in supersonic problems with shocks (10^{-6}~10^{-10}). IS_i is the smoothness measurement.

In order to make the nolinear scheme still pertain the same optimal order, i.e., 5th order, IS_i should have the property:

$$IS_k = C(1 + O(h^2)) \tag{3.9}$$

where C is the same number for three IS_i.

IS_i for 5th order WENO scheme has the following form:

$$\begin{cases} IS_1 = \frac{13}{12}\left(f_{j-2} - 2f_{j-1} + f_j\right)^2 + \frac{1}{4}\left(f_{j-2} - 4f_{j-1} + 3f_j\right)^2 \\ IS_2 = \frac{13}{12}\left(f_{j-1} - 2f_j + f_{j+1}\right)^2 + \frac{1}{4}\left(f_{j-1} - f_{j+1}\right)^2 \\ IS_3 = \frac{13}{12}\left(f_j - 2f_{j+1} + f_{j+2}\right)^2 + \frac{1}{4}\left(3f_j - 4f_{j+1} + f_{j+2}\right)^2 \end{cases} \tag{3.10}$$

The scheme for $h^-_{j+1/2}$ has a symmetric form of $h^+_{j+1/2}$ to the point $x_{j+1/2}$

Comparing to the standard 5th order WENO scheme discussed above, the 5th order Bandwidth-optimized WENO scheme uses one more point on the right, thus it has one more grid stencil [24],

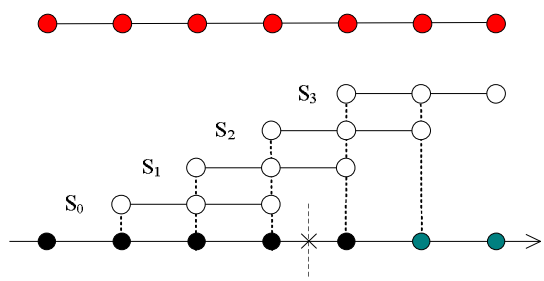

Figure 3.1 Grid Stencils for 5th Order Bandwidth-optimized WENO

Considering the positive flux, the four upwind-biased schemes on three candidates can be given as:

$$\begin{cases} h^{+\prime}{}_0 = \frac{1}{3}f_{j-2} - \frac{7}{6}f_{j-1} + \frac{11}{6}f_j \\ h^{+\prime}{}_1 = -\frac{1}{6}f_{j-1} + \frac{1}{3}f_j + \frac{5}{6}f_{j+1} \\ h^{+\prime}{}_2 = \frac{1}{3}f_j + \frac{5}{6}f_{j+1} - \frac{1}{6}f_{j+2} \\ h^{+\prime}{}_3 = \frac{11}{6}f_{j+1} - \frac{7}{6}f_{j+2} + \frac{1}{3}f_{j+3} \end{cases} \tag{3.11}$$

In the same way, we have,

$$h^{+}{}_{Linear,\, j+1/2} = \alpha_0 h^{+\prime}{}_0 + \alpha_1 h^{+\prime}{}_1 + \alpha_2 h^{+\prime}{}_2 + \alpha_3 h^{+\prime}{}_3 \tag{3.12}$$

when the optimal order is realized, the α_i must be determined as:

$$(\alpha_0, \alpha_1, \alpha_2, \alpha_3) = (0.05,\ 0.45,\ 0.45,\ 0.01) \tag{3.13}$$

The final nonlinear weighted schemes can be expressed as:

$$h^{+}{}_{j+1/2} = \omega_0 h^{+\prime}{}_0 + \omega_1 h^{+\prime}{}_1 + \omega_2 h^{+\prime}{}_2 + \omega_3 h^{+\prime}{}_3 \tag{3.14}$$

where

$$\omega_i = b_i / (b_0 + b_1 + b_2 + b_3) \tag{3.15}$$

$$b_i = \alpha_i / (\varepsilon + IS_i)^2 \tag{3.16}$$

IS_i has the following form:

$$\begin{cases} IS_0 = \dfrac{13}{12}\left(f_{j-2} - 2f_{j-1} + f_j\right)^2 + \dfrac{1}{4}\left(f_{j-2} - 4f_{j-1} + 3f_j\right)^2 \\ IS_1 = \dfrac{13}{12}\left(f_{j-1} - 2f_j + f_{j+1}\right)^2 + \dfrac{1}{4}\left(f_{j-1} - f_{j+1}\right)^2 \\ IS_2 = \dfrac{13}{12}\left(f_j - 2f_{j+1} + f_{j+2}\right)^2 + \dfrac{1}{4}\left(3f_j - 4f_{j+1} + f_{j+2}\right)^2 \\ IS_3 = \dfrac{13}{12}\left(f_{j+1} - 2f_{j+2} + f_{j+3}\right)^2 + \dfrac{1}{4}\left(-5f_{j+1} + 8f_{j+2} - 3f_{j+3}\right)^2 \end{cases} \tag{3.17}$$

In order to make the scheme stable, further modification is made as: $IS_3 = \max\limits_{0 \le k \le 3} IS_k$.

Further improvement for ω_k by Martin et al is:

$$\omega_i = \begin{cases} \alpha_k & if\ \max(TV_k)/\min(TV_k) < 5\ and\ \max(TV_k) < 0.2 \\ \omega_i & otherwise \end{cases} \tag{3.18}$$

where TV_k stands for the total variation on each candidate stencil.

As mentioned in Ref. 48, the large eddy simulation based on the WENO scheme was thought to be slightly more dissipative than other implicit LES methods. In order to reduce the dissipation of the scheme, the less dissipative Steger-Warming flux splitting method is used in the computation, instead of the commonly-used more dissipative Lax-Friedrich splitting method.

3.1.2 The Difference Scheme for the Viscous Terms

Considering the conservative form of the governing equations, the traditional 4th order central scheme (Equation (3.19)) is used twice to compute the 2nd order derivatives in viscous terms.

$$\left(\frac{\partial u}{\partial x}\right)_i = \frac{-u_{i+2} + 8u_{i+1} - 8u_{i-1} + u_{i-2}}{12\Delta x} \tag{3.19}$$

3.1.3 The Time Scheme

The basic methodology for the temporal terms in the Navier-Stokes equations adopts the explicit 3rd order TVB-type Runge-Kutta scheme [49]:

$$\begin{aligned} u^{(1)} &= u^n + \Delta t L\left(u^n\right) \\ u^{(2)} &= \frac{3}{4}u^n + \frac{1}{4}u^{(1)} + \frac{1}{4}\Delta t L\left(u^{(1)}\right) \\ u^{n+1} &= \frac{1}{3}u^n + \frac{2}{3}u^{(2)} + \frac{2}{3}\Delta t L\left(u^{(2)}\right) \end{aligned} \tag{3.20}$$

3.2 Grid Generation

In order to make comparison between the supersonic ramp flow with and without MVG control, two cases are designed. In the first case, the configuration consists of an MVG mounted upstream of the ramp (MVG-ramp) while the second configuration is a ramp without MVG control. Both the cases have the same streamwise and spanwise lengths. In order to preserve the accuracy of the geometry to reduce numerical errors as much as possible while using 5th order bandwidth-optimized WENO scheme, the strategy of body-fitted grids is adopted. Results in later parts of the paper testify that such grid frame is very helpful to obtain the high resolution of the flow structure.

The geometry of MVG is shown in Fig. 3.3. In order to alleviate the difficulty to grid generation caused by original vertical trailing-edge, a modification is made by declining the edge to 70°. The other geometric parameters in the figure are the same as those given by Babinsky[6], i.e., c=7.2h, α=24° and s=7.5h, where h is the height of MVG and s is the distance between the center lines of two adjacent MVGs. So the distance from the center line to the spanwsie boundary of the computation domain is 3.75h.

According to experiments by Babinsky [7], the ratio h/δ_0 of the models has the range from 0.3~1. The appropriate distance from the trailing-edge to the control area is around 19~56h or 8~19δ_0. So in this study, the height of MVG h is assumed to be $\delta_0/2$ and the horizontal distance from the apex of MVG to the ramp corner is set to be 19.5h or 9.75δ_0. The distance from the end of the ramp to the apex is 32.2896h. The distance from the starting point of the domain to the apex of MVG is 17.7775h. The height of the domain is from 10h to 15h while the width of the half domain is 3.75h. The geometric relation of the half of the domain can be seen in Fig. 3.4, where the symmetrical plane is the centre plane.

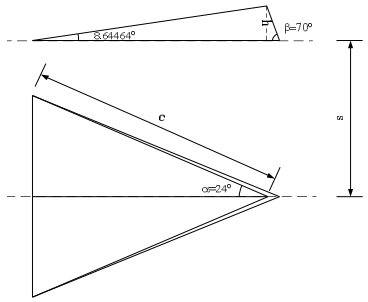

Figure 3.3 The Geometry of MVG

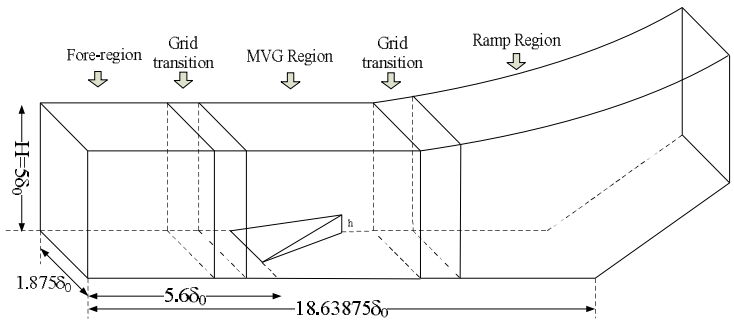

Figure 3.4 The Schematic of the Half Grid System of Case 1

Because the singularity of the geometry, it is difficult to use one technique to generate the whole grid system. A general grid partition technique is used in this grid generation. As shown in Fig. 3.4, three regions are divided as: the ramp region, MVG region and fore-region. Between each two regions, there is a grid transition buffer. Because of the symmetry of the grid distribution, only half of the grids need to be generated. The grid number for the whole system is: $n_{spanwise} \times n_{normal} \times n_{streamwise} = 137 \times 192 \times 1600$.

The grid generation includes two steps: first using analytical methods [22, 23] to generate the algebraic grids; next using elliptic grid generation equation to improve the orthogonal and smooth property of the grid.

The schematic figure can be shown in Fig. 3.5. The procedures for grid generation are: first generating the boundary grids of the lower and upper boundaries; next generating the inner grids by interpolation. Figure 3.6 shows the generated mesh with a grid interval of 8 in streamwise and of 6 in normal directions.

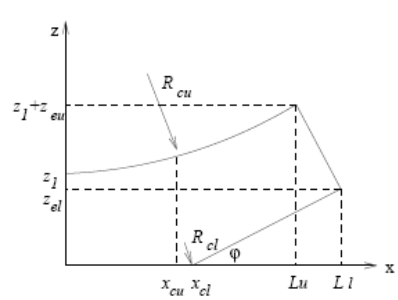

Figure 3.5 The Geometry Sketch of the Ramp

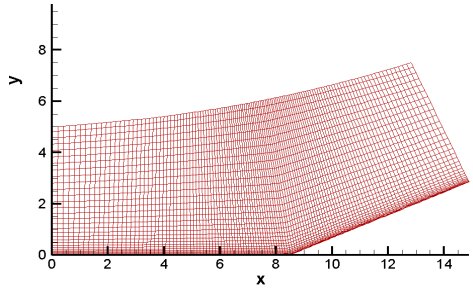

Figure 3.6 The Grid System of Case 1

Because of the specification of the boundary conditions on the body surface, an orthogonal grid is very important to ensure the high accuracy of the computation. This is particularly important to the case with complex geometry, where the zero normal gradient condition is usually realized by using the derivative along the normal grid line. To make grids orthogonal and smooth, a grid solver was developed by the group of the second author based on Laplace equations and algebraic transformations (see Ref. 50).

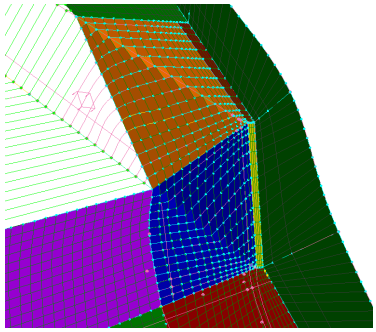

Figure 3.7 The Local View of Grids around the Trailing-edge

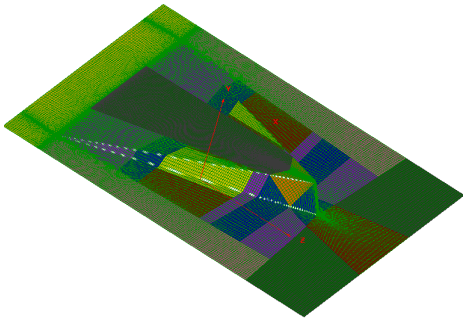

Figure 3.8 The Surface Grids of MVG in Patches

In order to generate the complete grids of MVG, it is essential to generate the surface grids. According to our experience, the quality of the surface grids will directly influence the quality of the 3-D volume grids, and the accurate description of the geometry by the surface grids can enhance the accuracy of the computation. Because the surface of MVG is of high singularity, it failed to use the automatic grid generation technique like projection by some commercial software. In this study, some manual work had to be done by the following steps: first a modification is made by smoothing the trailing-edge using a very small arc (see the yellow part in Fig. 3.7); next the surface is divided into many small patches so that the singularity of the shape is reduced in each patch; thirdly, the skeleton grid lines are constructed manually in the patch using some grid generation software in an interactive manner. Afterwards the lines are discretized into grid points. Careful adjustments are made to make the distribution of grids as smooth as possible; Finally, optimizations are made to let grid lines transit fluently between patches. The final surface grids can be seen in Fig. 3.8.

The final grids can be seen in Fig. 3.9-3.10. More details can also be found in Ref. 51.

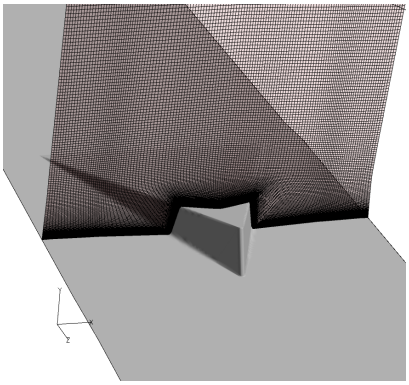

Figure 3.9 The Grids in Certain Cross-section

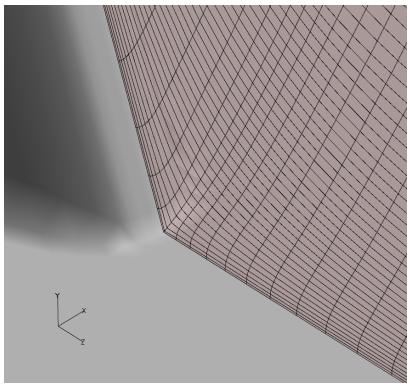

Figure 3.10 The Grids at the Foot of the Trailing-edge

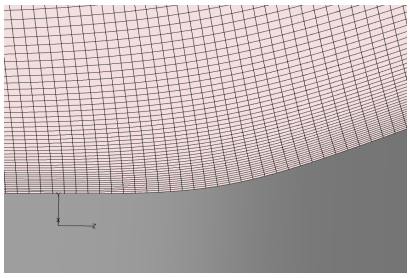

Figure 3.11 The Grids at the Ramp Corner

In order to make comparison with case 1, the grids of case 2 is generated by some modification to the grids of case1. Fig. 3.11 shows a local view of the grids at the ramp corner. Using the inflow flow profile described in the next section, a summary is given in table 1 about the geometric parameters of the grid system. Because the existence of MVG geometry, there are inevitable grid deformation and local clustering at the location where the shape changes discontinuously. To void such extreme cases, the grid intervals in wall unit are gauged at the entrance of the domain of case 1, the results of case 2 is the same as that of case 1.

Table 3.1 The Geometric Parameters for the Computation

L_x	L_y	L_z	Δx^+	Δy^+	Δz^+
$3.75\delta_0$	$5\text{-}7.5\delta_0$	$25.03\delta_0$	26.22	1.36-38.38	12.79

3.3 Boundary Conditions

The adiabatic, zero-gradient of pressure and non-slipping conditions are used for the wall as:

$$\partial T/\partial n = 0\ ,\ \partial p/\partial n = 0\ ,\ U=0 \tag{3.21}$$

The non-reflecting boundary conditions are applied for far field and periodic boundary conditions are adopted in the spanwise direction. No visible artificial reflections are observed by the shock waves.

It is a challenging topic about how to get fully developed turbulent inflow comparable to the experimental conditions? There is a large body of published work on generating turbulent inflow boundary condition for simulation of complex spatially developing external flows; the most representative paper is perhaps that of Lund, Wu & Squires (1998). Lund et al [52]. (1998) developed a simplified version of the Spalart method by invoking only the transformation on independent variables at two streamwise stations without altering the Navier-Stokes equations. This method and its subsequent variations have been shown to yield reasonable inflow conditions for complex, spatially developed flows because quite often the downstream pressure gradients and geometrical variations mask any major defects of the inflow. However, because of their semi-empirical nature, even with DNS resolution, it would be quite challenging for these methods to generate results that can be considered as experimental data quality for the turbulent boundary layer. Therefore, in present work, the turbulent mean profile and velocity fluctuations have been obtained from a separate DNS computation of compressible turbulent boundary layer.

The inflow conditions are generated using the following steps:

a) A turbulent mean profile is obtained from previous DNS simulation result from Ref. 53 for the streamwise velocity (w-velocity) whose distribution is scaled by using the local displacement thickness and free stream velocity. The DNS work was done for a laminar-turbulent transition on a flat plate with 60 millions of grids. The Reynolds number is 1000 based on the inflow boundary

layer thickness of displacement. At the first grid point in normal direction has $y^+ = 0.43$. The log law was checked and fully developed turbulent flow was confirmed to be obtained. The basic transfer is based on the assumption that the same distribution exists between the relation of $U/U_e \sim y/\delta^*$. The averaged streamwise velocity of MVG case can be got by smooth interpolation (3rd spline interpolation).

b) The pressure is uniform at inlet which is same as the free stream value. We treat the inflow pressure as a constant without fluctuations. The temperature profile is obtained using Walz's equation for the adiabatic wall:

The adiabatic wall temperature T_w is determined by $T_w = T_e\left(1 + r(\gamma - 1)/2 \times M_e^2\right)$, where the subscript 'e' means the edge of the boundary layer and *r* is the recovery factor with value 0.9. The temperature profile is obtained by Walz's equation,

$$T/T_e = T_w/T_e - r(\gamma - 1)/2 \times M_e^2 \left(U/U_e\right)^2 \tag{3.22}$$

c) The fluctuation components of the velocity are separated from the velocity at every instantaneous data file (total 20,000 files). The fluctuations are extracted by comparison of the mean flow and the instantaneous flow at each time step. The instantaneous data were recorded on three sections in the fully developed turbulent zone, which are used as the inflow data for the current work. Such fluctuations are rescaled in the same way. Because $\bar{T}/T_e = T_w/T_e - r(\gamma - 1)/2M_e^2\left(\bar{U}/U_e\right)^2$, we can get $d\bar{T} = -r(\gamma - 1)M_e^2 U d\bar{U}$ by ignoring the T_e and U_e in the non-dimensional form, or $\Delta T = -r(\gamma - 1)M_e^2 U \Delta U$. Density fluctuation is determined by $\frac{\Delta\rho}{\bar{\rho}} = -\frac{\Delta T}{\bar{T}}$.

d) Finally, the transformed parameters are $u = U + \Delta u$, $v = V + \Delta v$, $w = \Delta w$, $\rho = \bar{\rho} + \Delta\rho$, $p = \frac{\rho T}{\gamma M^2}$, $T = \bar{T} + \Delta T$.

Such inflow conditions are, of course, not the exact solutions of the Navier-Stokes equations. The flow solver will adjust and modulate the flow into fully developed turbulent flows while propagating downstream.

3.4 Code Validation

Because the 5th order bandwidth-optimized WENO scheme is a quite mature method and the problem studied in this paper contains shock waves, a supersonic inviscid flow around the half cylinder at M_∞=4 was selected as the validating test. The test can demonstrate the scheme's ability for shock capturing and confirm the correctness of the code system. Fig. 3.12 shows the isobar contour in the middle section in the spanwise direction, which indicates that the scheme can capture shock waves with essentially free of oscillations.

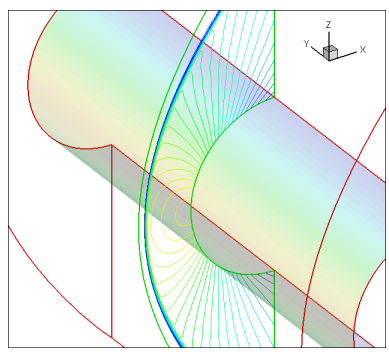

Figure 3.12 The Contour of the Pressure

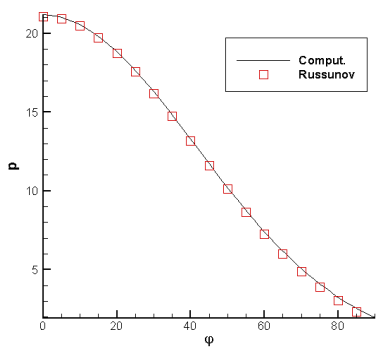

Figure 3.13 The Comparison of the Pressure

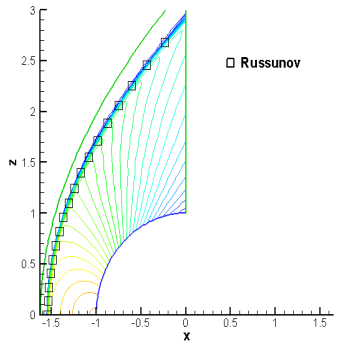

Figure 3.14 The Comparison of the Shock Location with that of Rusunov

Fig. 3.13 and 3.14 show the comparison between the numerical results and the asymptotic solution from Rusunov, which is usually considered as the “theoretical” solution of that problem. A good agreement is obtained between the two results. The convergence rate in Fig. 3.15 shows a reduction of about 6 orders of the residual was obtained.

Additional computations were made by rotating the curvilinear coordinates system alternatively to make the problem three-dimensional. The results prove the correctness of the current codes.

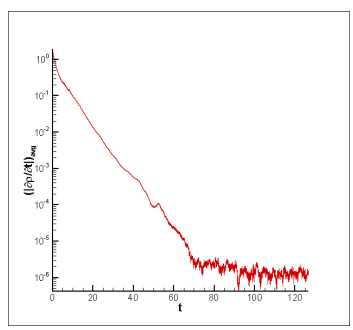

Figure 3.15 The Converging History of the 5th WENO Scheme

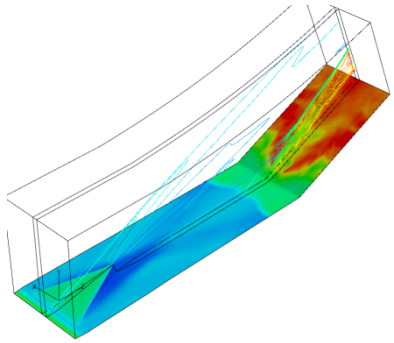

Figure 3.16 The Pressure Contour at the Central Plane and Body Surface

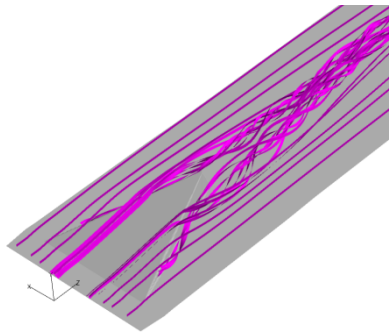

Figure 3.17 The Spatial Streamlines

Another small case is set up for computation on a MVG controlling laminar ramp flow with M=3 and Re_δ=4800, where a very coarse grid number was selected as $n_{streamwise}\times n_{normal}\times n_{spanwise}$=420×121×64. The purpose of that test is to check if the computation can qualitatively capture the main flow structures of the problem. It can be found in Fig. 3.16 that the main shock and expansion waves are captured by the simulation; the reflecting shock wave generated by ramp is clearly distinguished as well. There is a hint about the possible re-compression shock wave. The pair of primary counter-rotating streamwise vortices is visualized by streamlines in Fig. 3.17. The preliminary results show that the main flow structures qualitatively agree with the results by Babinsky [7]. So this means the primary structures are captured and correctly described by the computation qualitatively, although there are few small scaled structures lost due to the reason that the grids are too coarse. The code system can be

used for the subsequent LES with much more grids. The validation made here is just for evidence that out LES code and scheme are correct for the Euler solver. The further validation for SBLI is made for a compression corner by comparing our LES results and experimental results [7,17] (see Figures 3.18 and Figures 3.19). We believe it is better to compare our LES results with experiment for the validation purpose.

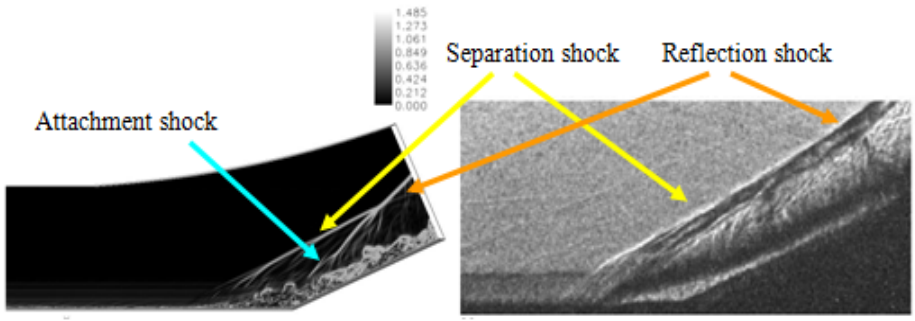

(a) (b)

Figure 3.18 (a) The Instantaneous Digital Schlieren at Central Plane (ramp angle is 24 degree) and (b) The Schlieren Pictures from the Experiment (ramp angle is 25 degree)

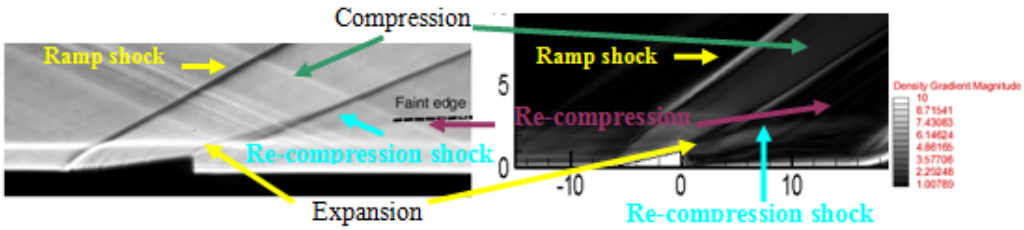

Figure 3.19 (a) The Schlieren Picture from Babinsky and (b) The Numerical Schlieren Picture at the Central Plane

CHAPTER 4

NUMERICAL RESULTS FOR SUPERSONIC RAMP FLOW

4.1 Inflow Boundary Layer Profiles

The inflow profiles are checked ahead of the MVG after long periods of computation. In order to define a reference coordinate system in this and following sections, the apex of the MVG is selected as the original point. The section for checking is located at 11.97h from the inlet in the streamwise direction. At this section, the Pitot pressure recovery coefficient and incompressible shape factor H_i are calculated and averaged in the spanwise direction. The Pitot pressure recovery coefficient used in this work is defined as:

$$C_{Ptot_{rc}} = (1/H)\int_0^H (p_0/p_{0\infty})dy \tag{4.1}$$

where H can be a value approximately as the height of the domain. The definitions of displacement thickness (δ*) and momentum thickness (θ) are given as:

$$\begin{cases} \delta^* = \int_0^H (1-U/U_\infty)dy \\ \theta = \int_0^H (U/U_\infty)(1-U/U_\infty)dy \end{cases} \tag{4.2}$$

Here, the averaged $C_{Ptot_{rc}}$ is 0.9912, and the averaged $H_i = \delta^*/\theta$ =1.35. As well known, the H_i for the laminar flow is around 2.6 and for the standard turbulent flow is about 1.2~1.4. So, the results indicate that the methods described in Chapter 3 produce a fully developed turbulent inflow.

Fig. 4.1 shows the inflow boundary layer velocity profile in log - coordinates. There is a well-defined log region and the agreement with the analytical profile is well throughout. These

results are typical for a naturally grown turbulent boundary layer in equilibrium (see Guarini [54] et al).

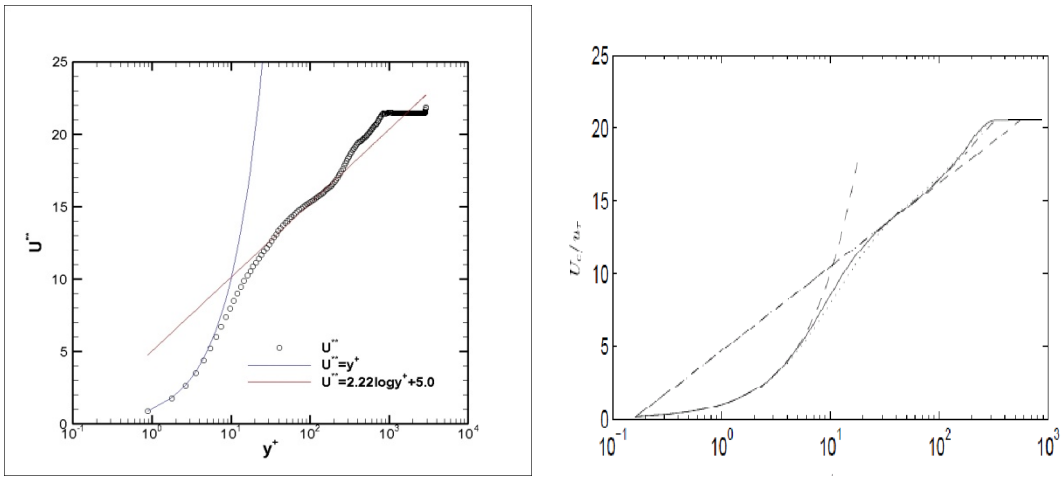

(a) (b)

Figure 4.1 Inflow Boundary-layer Profile Comparison with GUARINI et al's (a) Inflow Velocity Profile by Our Computation (b) Inflow Velocity Profile by Guarini [54] ($U^{**} = 2.5\log y^{+} + 4.7$)

4.2 Results of the Supersonic Ramp Flow (without MVG)

For comparison with the MVG-ramp flow, the computation is made first on the ramp flow without MVG.

4.2.1 Flow Structures of the Instantaneous and Averaged Flow

A typical instantaneous flow structure is shown in Fig. 4.2 using certain instantaneous data. The basic shock structures are comprised of the separation shock and the reflection shock by the ramp. The compression or weak waves generated in the region of separation are a result of the gradual thickening of the boundary-layer before it finally separates and not just because of the flow fluctuations generated by the convective structures. In fact the fluctuations of these weak waves are a result of the breathing motion of the separation bubble. Further a reattachment shock is also formed on the ramp section. The separation and reattachment shocks merge over the ramp into a single reflection shock.

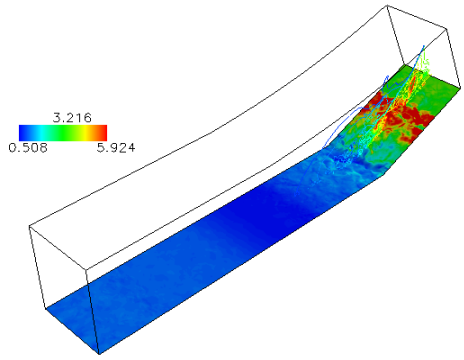

Figure 4.2 The Pressure Contour at the Central Plane and Body Surface

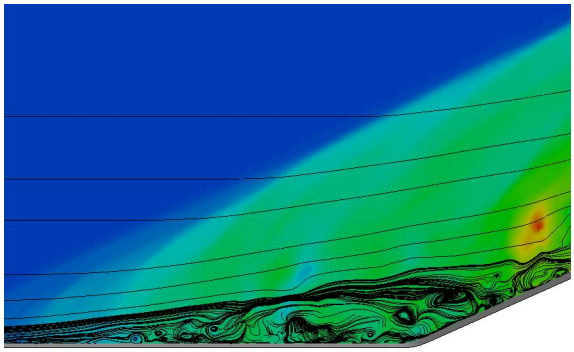

Figure 4.3 The Cross-section Streamlines at the Central Plane

The surface and cross section pressure contour clearly illustrate that the flow demonstrates turbulent features qualitatively within and after the separation. This infers that the separation has the effect on amplification of turbulence. It is believed that the recirculation of the flow makes the fluctuations reiterate within a finite region and develop nonlinearly. From the numerical simulation, it can be found that from the development of the separation flow, the initial structures are quasi two-dimensional (2-D) for spanwise vortices; however, when the upstream three-dimensional (3-D) disturbances arrive, the flow quickly becomes three dimensional. The instantaneous vortex structure in the separation zone appears to contain several large vortices accompanied by many small ones, as shown in Fig. 4.3.

The instantaneous numerical schlieren image of the central plane is given in Fig. 3.18(a), which uses the value of $|\nabla\rho|$. In order to get the clear picture of the structures, only the small value region is used for visualization. For qualitative comparison, an experimental picture of ramp flow at M=2.9 with large Reynolds number is given in Fig. 3.18(b) obtained from the experiment by Zheltovodov [19]. The experimental picture should be spanwise averaged in the path of the light and time averaged due to the film exposure so that less tiny structures can be observed. The comparison of experimental and LES results shows they are not exactly same, but pretty much have similar structure. From both pictures, we can observe that the separation shock wave has a declining angle which is a little lager but nearly same to the ramp angle which is almost aligned with the reflection shock (which is more obvious in the picture of the experiment); complex compressive waves are generated underneath the shock by vortices in the boundary layer. In contrast to the case of the laminar flow, the separation shock is completely separated from the reflection shock with an angle which is much smaller than the ramp angle.

4.2.2 The Length of the Separation Zone by SBLI

The size of the separation is illustrated by the length from the start of the separation to the ramp corner. Because the attachment position from the statistic results of the MVG-ramp flow is still scattering, the length from the attachment to the corner is not considered here temporarily. The determination about the position of the separation uses surface-limiting streamlines and further validated by the rising position of the pressure distribution. Finally, the length is estimated at around 4.1~4.2δ_0, which is in consistency with that of P. Martin [24], i.e., 4.2δ_0.

4.2.3 The Quality of the Downstream Boundary Layer After the Separating Corner

The averaged data at the location $1.07\delta_0$ in font of the outlet along the ramp surface is used to make analysis of the characteristics of the boundary layer. The incompressible displacement thickness, momentum thickness and shape factor are calculated based on the time-averaged flow field. The definitions for the thickness can be seen in Equation (4.2), "H" in the equation is selected as a height within the reflection shock wave, and "U_∞" uses the value after the shock wave, i.e., $(w/U_\infty, v/U_\infty)$=(0.7384, 0.292). The final results are: the incompressible displacement thickness is $0.694615\delta_0$, the incompressible momentum thickness is $0.463510\delta_0$, the shape factor H_i is 1.49860. The Pitot pressure recovery coefficient is about 0.787.

4.3 Results of the MVG Controlled Ramp Flow

As already mentioned, numerical simulations are made with M=2.5 and Re_θ=5760, but the experiment of Babinsky has a much larger Re_θ, i.e., about 28800. So the comparison between the computation and experiment in this paper should mainly be qualitative.

4.3.1 Velocity Profile Behind MVG

Fig. 4.4 gives a qualitative comparison with experiment (Babinsky et al [7], 2009) in the time and spanwise averaged velocity profile behind MVG. Qualitative agreement is achieved.

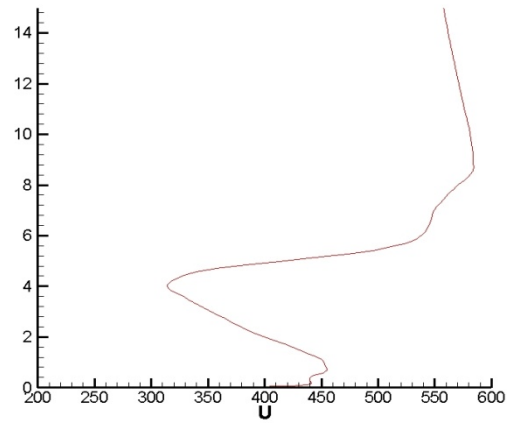

(a)

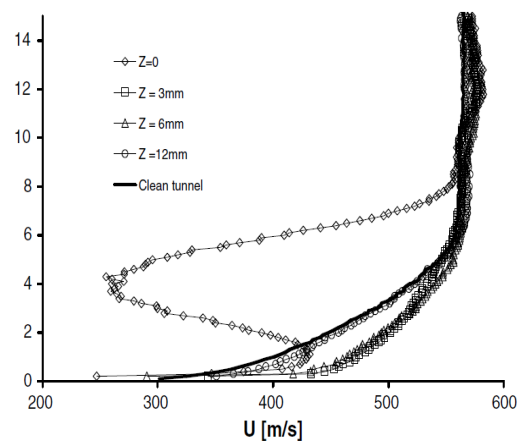

(b)

Figure 4.4 Qualitative Comparison of Averaged Velocity Profile behind MVG with Experiment (a) Averaged Velocity Profile behind MVG (b) Averaged Velocity Profile by Babinsky et al

4.3.2 The Three Dimensional Shock/Expansion Wave System of the MVG-ramp Flow

Because of the supersonic boundary layer inflow, it is expected that MVG will lead to strong disturbances like shock waves. Based on the schlieren picture of the experiment, Babinsky [7] presented the structure of the wave system, i.e., the first reflection shock, the expansion wave system and the re-compression shock, as shown in Fig. 3.18a. The first shock will bend within the incoming boundary layer due to “the change in Mach number”, and “a second shock wave then turns the flow back to horizontal”. A subtle oblique “λ” structure is

observed at the foot of the re-compression shock from the picture. In Fig. 3.18b, we present the numerical schlieren picture of the time-averaged flow field at the central plane. In the figure, the two shock waves are well described by the computation. The bending of the main shock to the wall can be distinguished; the oblique "λ" structure can be found on the foot of the second shock as well. The measured shock angles from Babinsky's experiment are: 26.869° for the first shock, and 21.93° for the re-compression shock. In contrast, the computational values are: 26.988° for the first shock, and 24.656° for the re-compression shock. Considering the declining angle of the trailing-edge is 70°, not the 90° as in the experiment, the computational results show a reasonable agreement with experiment. Note that the experiment work does not include a ramp, but the computation does.

Although the clear presentations are given by both experiment and computation, there is no available information about the possible 3-D structure of the shocks which will be given below. In Fig. 4.5, the spatial structures of the wave system are given by instantaneous cross-section pressure contours. From the first section in Fig. 4.5, the wave system is found to be the main MVG ramp shock wave and the expansion wave emanating from the edge of the MVG. The remaining sections show an arc-like structure of the re-compression shock wave, which is located behind the MVG ramp shock wave. The size of the arc keeps growing while moving downstream. The curve shape of the re-compression shocks implies the function of the re-compression shock wave is to make the expansion flow satisfy the "virtual" boundary condition created by the streamwise vortices, at least at the initial stage of the formation of the shock wave. Detailed investigations show that, the head and feet of the arc-like shock are separated from each other in the initial stage (see Fig. 4.6a). They begin to connect to form a complete arc curve at a certain downstream location, as shown in Fig. 4.6b. The mechanism about this phenomenon will be discussed in the next sub-section.

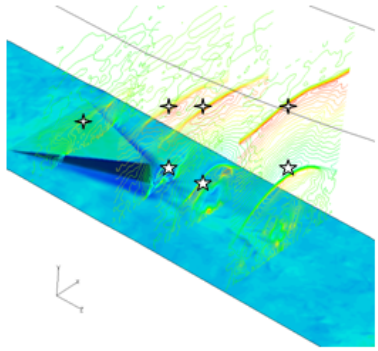

Figure 4.5 The Overview of the 3-D Structure of the Shock Waves

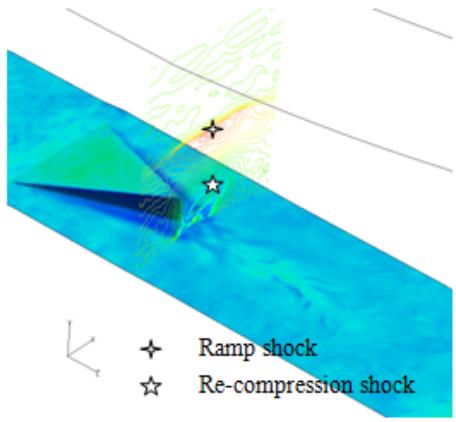

(a)

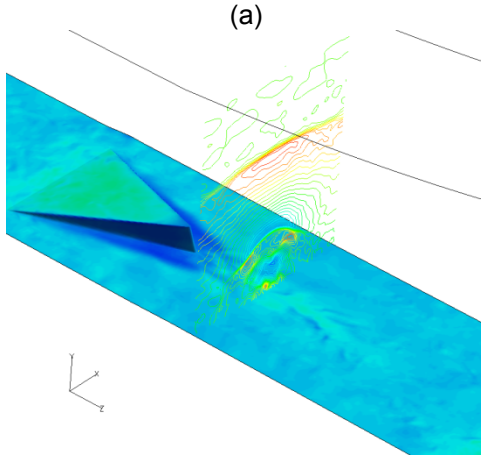

(b)

Figure 4.6 The 3-D Structure at the Inter-mediate Section 1 (a) and 2 (b)

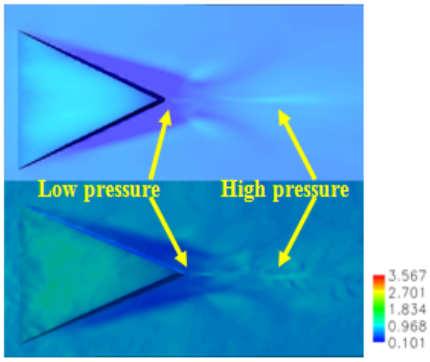

Figure 4.7 The Time-averaged (upper) and Instantaneous (lower) Surface Pressure

Fig. 4.7 shows the surface pressure structure by the time-averaged and instantaneous surface pressure contour respectively. From these figures, the surface pressure structure can be described: there are low pressure regions on both sides of the MVG, which obviously results from the suction effect of the primary streamwise vortices. After the foot of the trailing-edge, there is an isolated high pressure region, which corresponds to the stagnation point of the flow near the wall. Afterwards there is a pair of oblique high pressure slots, which are followed by low pressure slots. In the region around the center line, another high pressure region (in the sense of average) appears again. The mechanism about the structures will be discussed in the next sub-section.

4.3.3 The Topology of the Separation and Vortices of the MVG Flow

From the experiment of Babinsky [7], useful information is given by surface oil flow. For comparison, the pictures of the surface oil flow from experiment and limiting streamlines from the computation are given in Fig. 4.8-4.9. The topology of the two figures is essentially the same. The separation lines of the horseshoe vortex, the secondary separation lines beside the MVG and the ones after the MVG are clearly described by computation. Such lines are the most obvious traces found in experiment due to the deposit of the oil. Some differences exist

between the computation and the experiment. The biggest difference between the results is that, the separation ahead of the MVG in experiment is smaller than that of computation. The reason might be that the Reynolds number in computation is not as large as in experiment. The horseshoe vortex in computation has a stable or a little shrinking region, whereas the region in experiment seems to be enlarged beside the MVG.

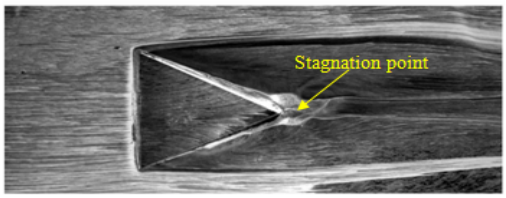

Figure 4.8 The Surface Oil Flow by Babinsky

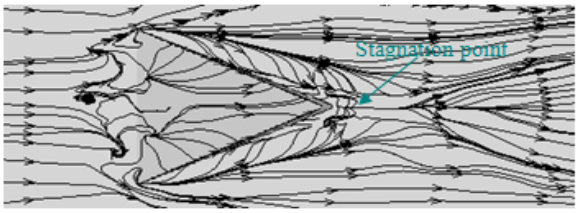

Figure 4.9 The Surface Limiting Streamlines by Computation

In order to explore the mechanism of the separation topology, further investigations are made on the separation pattern at the end and the side of the MVG. In Fig. 4.10 and 4.11, surface limiting streamlines are depicted on the wall surface. It can be seen that the separation pattern of the primary streamwise vortices is an open-typed separation (see Fig. 4.11(a)). The separation lines locate on the upper edge of the MVG and end at a degenerate nodal point (NP) near the top of the MVG. This indicates that the separation completely departs form the surface and becomes a fully three-dimensional separation. Beside the MVG, there are two pairs of secondary separations, the one lies on the bottom wall, and the other lies on the side of MVG. Both separations are open-typed dominant ones and ended in spiral points (SPP). This also implies the end of the surface separation and the lift up of secondary vortices. After that, there is a newly generated pair of secondary separation on the bottom wall surface after MVG, which is

started from a pair of saddle points (SDP). After the trailing-edge, there is a source-typed nodal point (NP) on the wall, which corresponds to the stagnation point in the back dead-air region. There are other small separations as well, like the ones started form saddle points and ended in spiral points. Their length scale is in general quite small and they are thought to play a minor role.

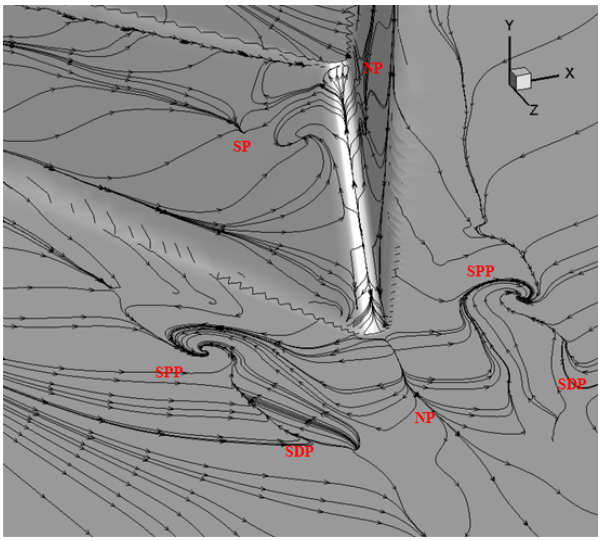

Figure 4.10 The Separation Pattern near the end of MVG

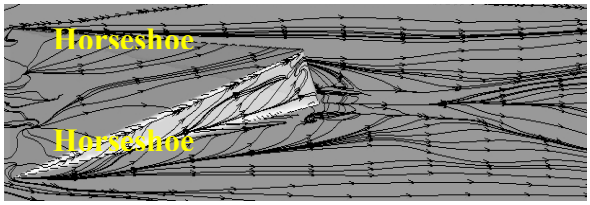

(a)

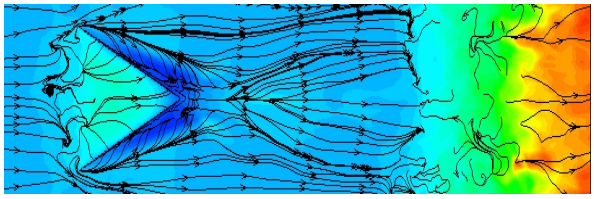

(b)

Figure 4.11 The Various Views of Surface Separation Pattern (SSP) a) SSP on the Side of MVG b) SSP Backgrounded using the Pressure Contour

In summary, according to the above analyses, a dynamic vortex model can be obtained and shown in Fig. 4.12 in the one-half of the symmetric domain: there are mainly 5 pairs of vortices in the flow field near MVG, i.e., one pair of horseshoe vortices; one pair of primary vortices by inflow separation beside the MVG; two pairs of secondary vortices on the side of MVG and underneath the primary vortices, which will leave the body surface later to become fully 3-D separations by the way of spiral points in the body surface, and interact with the primary vortices when propagating downstream; and one pair of newly generated secondary vortices above the bottom wall surface, which are located after the dead-air region behind the MVG and caused by the strong primary vortex.

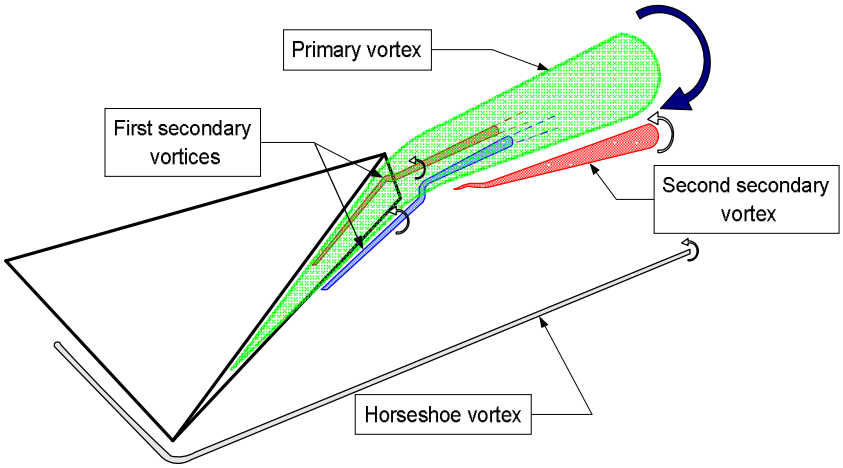

Figure 4.12 The Dynamic Vortex Model

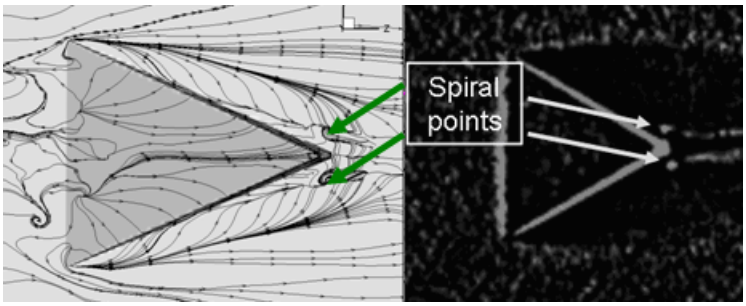

Figure 4.13 The Comparison between the Computation and the Validating Experiment

This 5-pair-vortex model near MVG is different from the one reported in Ref. 7 by Babinsky. The difference mainly exists in the secondary vortex structures. In Ref. 6, the first secondary beside the MVG and the new secondary vortex under the primary vortices in Fig. 4.12 were thought to be the same vortex, while the current model shows the first one will end in a pair of spiral points, lift up and mix with the primary vortices, while a pair of new secondary vortex will be generated under the primary ones. So the critical point to validate the current model is the existence of the spiral points due to the surface separation. Recently in April 2010, after being told the predictions and required for validation about the spiral points, the experimentalists at the University of Texas at Arlington (UT Arlington) repeated their experiment at the same Mach number [56,57]. Instead of only checking the oil flow after the run of the wind tunnel, they took a video from the top view to record the process of the MVG oil flow. A distinct pair of oil accumulating points was found in the video (see the experimental snapshot in Fig. 4.13). The points just correspond to the spiral points, and this verification justifies the vortex model presented in the paper.

Surface separation pattern can explain the surface pressure structure to some degree. Around the stagnation point at the end of MVG, the flow moves down while decelerating towards the wall. This process will transfer the kinetic energy to the potential energy of the fluid, i.e., reduction of velocity results in the increase of the pressure. That's why there is a high pressure spot at the centerline after the MVG (see Fig. 4.7 and 4.11(b)). The fact that the secondary separations beside the MVG end in spiral points indicate the secondary vortexes will lift up and interact with the outer high speed flow. This interaction will decelerate the fast flow and lead to compression. In the supersonic flow, the disturbances will produce a shock wave, which propagates approximately along the Mach line, and result in a pair of high pressure slots. The re-acceleration of the flow after the compression generates the accompanied low pressure slots. The structures of the surface pressure show a reasonable correspondence to the flow structure.

In order to study the 3-D structures of the vortices, the cross-section streamlines are drawn at several sections with constant streamwise grid indices, as shown in Figs. 4.14-4.19. The streamwise positions of the cross-sections are $L_{from\ apex}/h \approx 1.15$, 3.04, 6.45, 14.95, 18.78 and 27.41, where $L_{from\ apex}$ is the streamwise distance measured from the apex of MVG. The time-averaged velocity field is used for drawing streamlines, and the streamwise velocity contour is used for background. From these figures, it can be seen that: a) the so-called momentum deficit is related to the streamwise vortices, which will be discussed later; b) the streamwise vortices initially locate in a lower position, but then gradually lift up when propagating downstream. Secondary vortices are observed under the primary ones. The result is in consistency with the referenced computations and experiments. The mechanism is thought to be the "upwash" effect induced by the vortex; c) the streamwise vortices are not symmetric to the central plane in the downstream position. The asymmetric leeward separation flow occurs elsewhere in fluid dynamics, like that of the slender body at high attack angle, where the mechanism is thought to be the structural instability of the cross-section topology. Further knowledge is recommended to related references; d) the streamwise vortices become weak when moving downstream and further degenerate within the SBLI region (see Fig. 4.18). After that location, there is a recovery about the vortex structure, as shown in Fig. 4.19, but the circular cross-section streamlines do not mean the existence of a strong vortex.

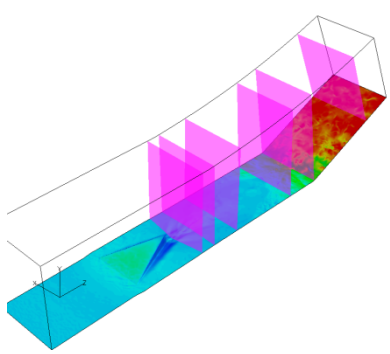

Figure 4.14 The Locations of the Cross Sections ($L_{from\ apex}/h \approx 1.15$, 3.04, 6.45, 14.95, 18.78 and 27.41)

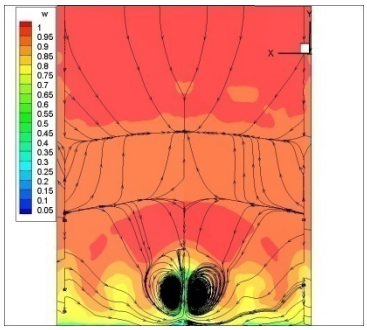

Figure 4.15 The Streamlines at Cross Section 2

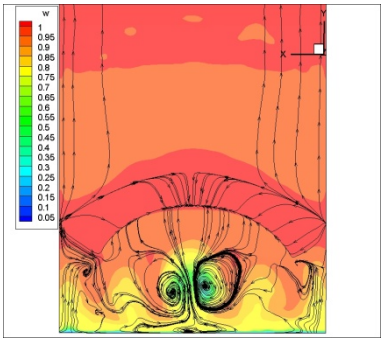

Figure 4.16 The Streamlines at Cross Section 3

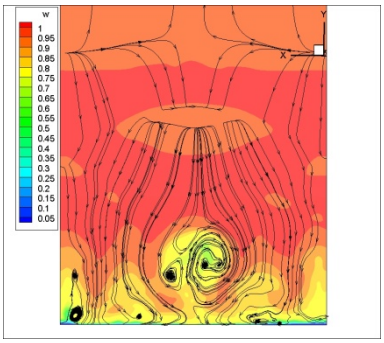

Figure 4.17 The Streamlines at Cross Section 4

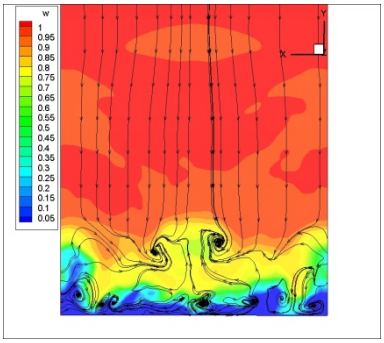

Figure 4.18 The Streamlines at Cross Section 5

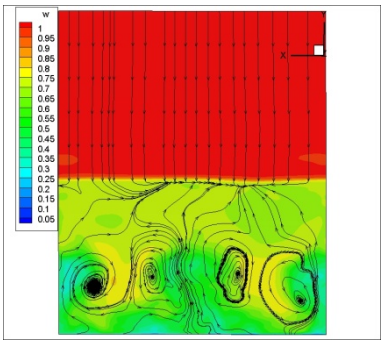

Figure 4.19 The Streamlines at Cross Section 6

4.3.4 The Formation of the Streamwise Momentum Deficit After the MVG

The momentum deficit is a unique phenomenon which was first observed in the experiment by Babinsky [7], which is later confirmed by the computation of Ghosh, Choi and Edwards [8] and Lee [9]. For clarity, the typical structure of the deficit is shown again in Fig. 4.20 using the averaged streamwise velocity at Section 2 in Fig. 4.14. In the region near MVG, the shape of deficit appears to be a circle, with a root connected to the boundary layer usually (mushroom shaped). Underneath the circle, there are two high streamwise velocity regions. About the mechanism of the deficit, Babinsky thought it is the wake of MVG, and Lee only mentioned “the two vortical tubes merge together to create a larger tube with two counter-rotating vortices inside”. What is the relation of the deficit to the flow structure? What does the low speed flow come from? The existing explanations did not provide a clear mechanism about the formation of the deficit.

In order to investigate the origins of the deficit, a heuristic analysis is made by investigating specific streamlines that are defined in certain cross-sections of the momentum deficit. Firstly, a cross-section after the MVG is selected as a reference plane as shown in Fig. 4.21, in which the momentum deficit on the plane is shown by using the contour of the instantaneous streamwise velocity, which appears in a green circular region. Next, we put some seeds around the boundary of deficit and within the deficit. Then we draw the 3-D streamlines starting from the seeds in both backward and forward directions. Because the seeds surround

or locate within the deficit, the distribution of the backward streamlines qualitatively reflects the origins of the deficit. It can be seen from Fig. 4.21 that: a) all backward streamlines rotate around the primary streamwise vortex, which indicates the formation of the deficit is caused by primary vortices; b) all backwards streamlines come from the upper surface of the MVG, which indicates the main source of the deficit is the shedding of the upstream low-speed boundary layer, but is not the boundary layer flow around the MVG and after the MVG.

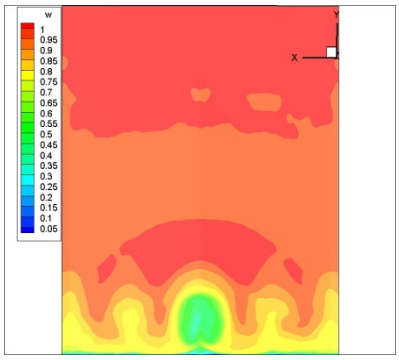

Figure 4.20 The Contour of the Averaged Streamwise Velocity at Section 2

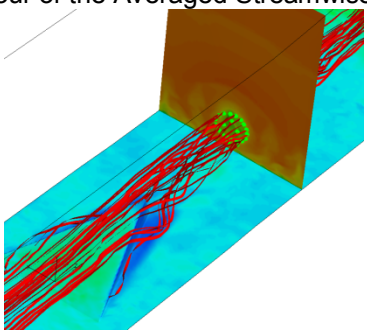

Figure 4.21 The Spatial Stream-lines passing through the Boundary of Deficit

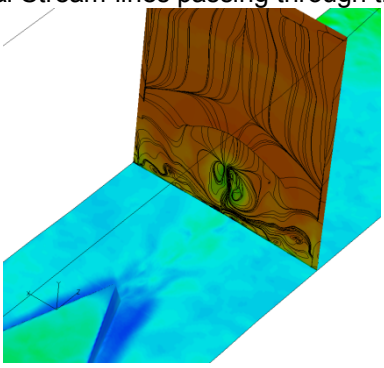

Figure 4.22 The Cross-section Streamlines

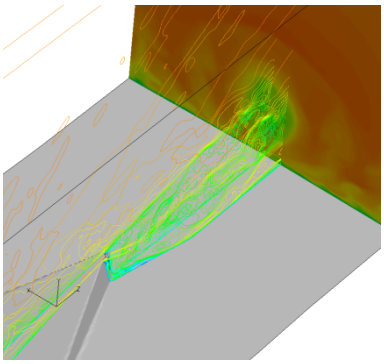

Figure 4.23 The Streamwise Velocity Contour at two Streamwise Computational Planes

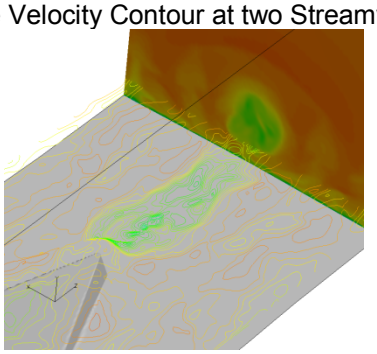

Figure 4.24 The Streamwise Velocity Contour at a Horizontal Computational Plane

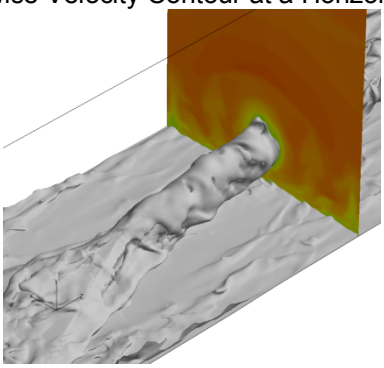

Figure 4.25 The Iso-surface of the Streamwise Velocity

To further validate the first conclusion given above, the cross-section streamlines are drawn at the same section as shown in Fig. 4.22, where the aforementioned seeds are drawn to show the boundary of the deficit. The results show that there is a pair of counter-rotating vortices, and the deficit is approximately within the vortex region.

We also draw streamwise velocity contours in the streamwise and horizontal computational sections, as shown in Figs. 4.23 and 4.24. From these figures, it can be found

that: a) the slow fluid in deficit is mainly the results of the shedding of the upstream MVG boundary layer, but not the ejection from the bottom of the local boundary layer through the so-called mushroom mechanism; b) the boundary layer in outer spanwise location will be carried along by vortices into region closer to the center line. That is why the streamwise velocity contour in Fig. 4.24 seems to start from a finite distance after MVG. This phenomenon is also consistent with the trace of the spatial streamlines in Fig. 4.21. At last, an iso-surface of streamwise velocity is drawn in Fig. 4.25 by choosing a value of the deficit at its boundary. The surface wraps the MVG and forms a distorting cylinder, i. e., the 3-D surface of the deficit. The results again agree with the above two conclusions.

4.3.5 Vortex Rings - A New Mechanism in MVG-ramp Flow Control

According to the up-to-date knowledge from the experiment and computation, a pair of primary counter-rotating streamwise vortices and the underneath attached secondary ones are considered to be the mechanism of the flow control. The primary vortices will bring about high speed momentum entrainment to the location near to the floor [9], which is favorable to resistance of the adverse gradient of the pressure. According to our computation and the results from other authors [8], the rotation of the streamwise vortices becomes weak quickly (see Fig. 4.26) and streamlines oscillate in the space due to the shear layer instability around the momentum deficit circle. It suggests that there might be some other mechanism in the MVG controlled flow, besides the only pair of streamwise vortex tubes to cause the momentum exchange.

Because the vortex axis is usually the location with the minimum pressure, the iso-surface of pressure is an easy tool to visualize the vortex tube. In Fig. 4.27, we draw the iso-surface of pressure using the same instantaneous data as that of Fig. 4.26. Besides the expansion wave and the surface wrapping the tube near the trailing-edge, the ring-like structures are found in the subsequent downstream region. Such rings appear initially not far

away from the trailing-edge, and become larger and irregular when moving downstream; in the meanwhile the streamwise vortex tubes become weaker and less observable at certain locations.

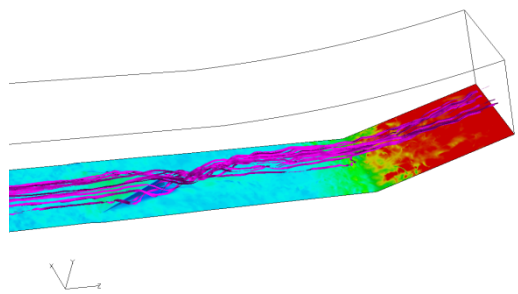

Figure 4.26 The Instantaneous Spatial Streamlines

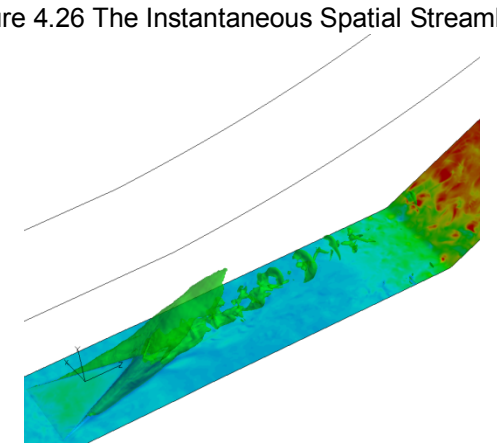

Figure 4.27 The Iso-surface of the Instantaneous Pressure

To investigate the vortex structure within and after the separation, a technique [55] is used by the iso-surface of the λ_2, which is the second eigenvalue of the 3×3 matrix comprised of velocity gradient, i.e., $M_{ij} = \sum_{k=1}^{3}\left(\Omega_{ik}\Omega_{kj} + S_{ik}S_{kj}\right)$ where $S_{ij} = 1/2\left(\partial u_i/\partial x_j + \partial u_j/\partial x_i\right)$ and $\Omega_{ij} = 1/2\left(\partial u_i/\partial x_j - \partial u_j/\partial x_i\right)$. A small negative value is selected for visualization. It can be seen from Fig. 4.28 and 4.29 that there are a large amount of vortices with various length scales in the concerned region in which many of them are streamwise vortices. Moreover, hairpin vortices with ring-like head are found within the vortices. The absence of the inflow vortices at the

selected iso-surface value means that the intensity of the vortices is stronger in the separation zone. This provides an indirect proof of the amplification of the fluctuation by the flow separation.

The well-shaped rings are approximately perpendicular to the flat plate, and then begin to deform while propagating downstream. Finally, they hit the separation shock of SBLI and strongly interact with the separation shock. The lower part of the ring first hits the shock and the speed decelerates. Next, the upper part of the ring hits the shock. So the vortex rings on the ramp appear in an oblique posture. The rings maintain their existence until flowing out of the domain.

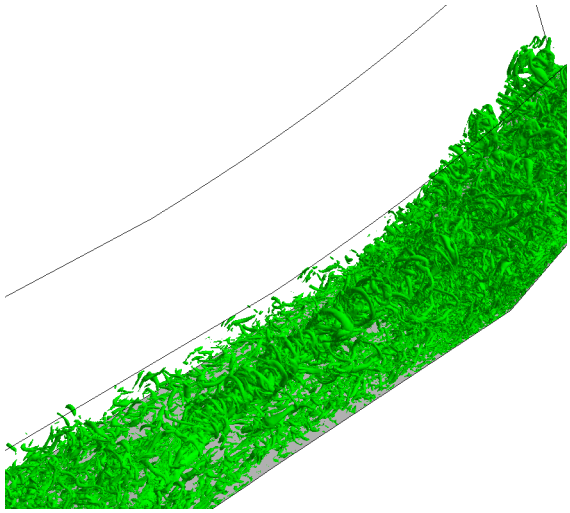

Figure 4.28 Vortex Rings shown by the Iso-surface of λ_2

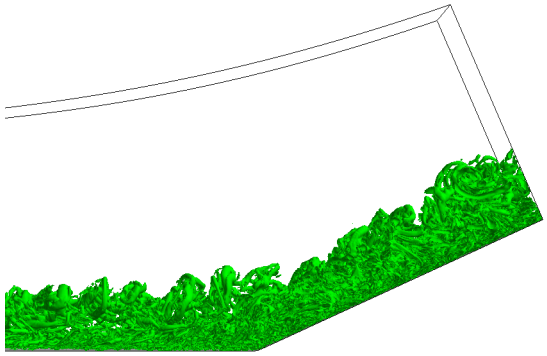

Figure 4.29 The Side View of Vortex Rings on the Ramp

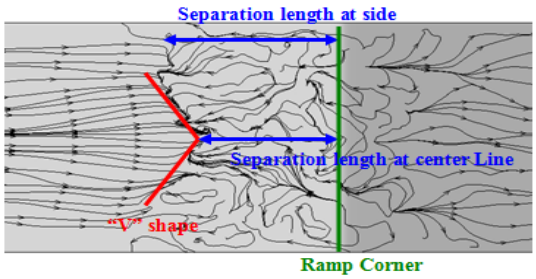

Figure 4.30 Surface Limiting Streamlines at SBLI Region

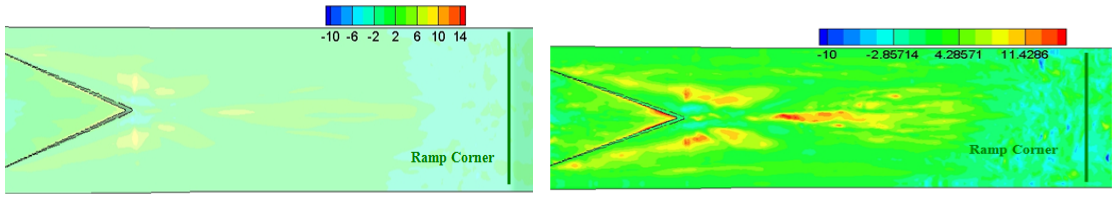

Figure 4.31 The Time-averaged (left) and Instantaneous (right) Friction Coefficient Distribution at SBLI Region.

4.3.6 The Characteristics of the Separation and the Comparison with the Ramp Flow without MVG

Fig 4.30 gives the time-averaged surface limiting streamlines at SBLI region. Fig. 4.31 shows the The time-averaged (upper) and instantaneous (lower) friction coefficient distribution

at SBLI region. Because the attachment location is difficult to determine, the size of the separation is illustrated by using the length from the start of the separation to the ramp corner as defined before. From the figure, the shape of the separation zone looks like the “V” shape, the length of the separation at the two spanwise sides of the domain is estimated to be around 6~6.5*h* and the length at the center line is estimated to be around 5*h*. Compared with the value 8.2~8.4*h* (4.1~4.2δ_0) for the ramp only case, MVG distinctly reduces the length of the separation region. In Fig. 4.32, a comparison is given on the distribution of the time-averaged streamwise velocity of the two cases. The location of the distribution is on the center line and 4.5663δ_0 in front of the ramp corner. Although there is a dent in the distribution of MVG-controlled flow due to the momentum deficit, the shear of the streamwise velocity at the bottom of the boundary layer of case 1 is higher than that of the ramp flow without MVG. And as we know, larger streamwise velocity is favorable to separation resistance. In a recent paper [58], Manchester, Manisankar et al using micro ramps on a 24deg. compression ramp model (M=2.0) gave a possible explanation leading to the formation of corrugations with such flow control devices (that generate streamwise vortices). Further they also observed formation of striation pattern on the ramp surface with control.

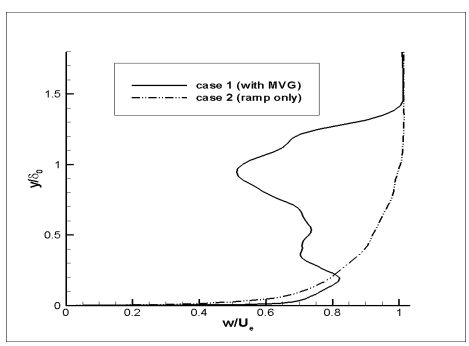

Figure 4.32 The Distribution of the Time-averaged Streamwise Velocity of the two Cases

4.3.7 The Quality of the Downstream Boundary Layer and the Effect of the Control

Using the same method in Eq. 4.1 and 4.2, the incompressible displacement thickness, momentum thickness, shape factor and the Pitot pressure recovery coefficient are calculated at

the same section based on the time-averaged data. For comparison, we use the same value of "U_∞" as is used in Eq. 4.2. The final results are: the incompressible displacement thickness is 0.678847δ_0, the incompressible momentum thickness is 0.489646δ_0, the shape factor H_i is 1.38640, and the Pitot pressure recovery coefficient is about 0.649. The results show that the MVG-ramp flow has a better shape factor but a lower Pitot pressure recovery coefficient compared to that of the ramp only case. Fig. 4.33 shows the centerline mean wall pressure distribution after the MVG for both cases.

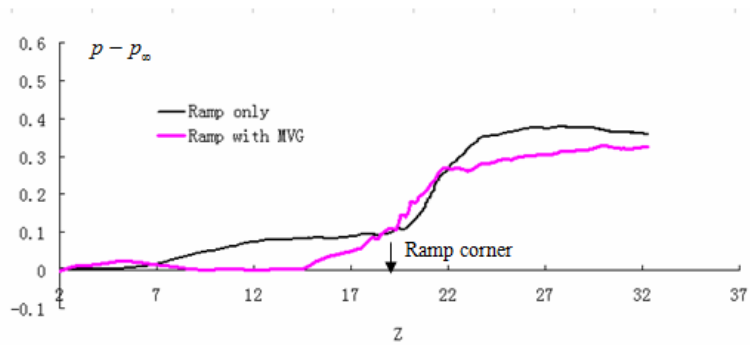

Figure 4.33 Comparison of the Mean Wall Pressure Distribution at the Centerline after the MVG (both on the base plate and the ramp surface).

CHAPTER 5

NUMERICAL STUDY ON THE MECHANISM OF VORTEX RINGS

5.1 Vortex Ring Structure

The rings are generated almost erectly at first and then be continuously distorted and enlarged while propagating downstream. These rings could be a dominant factor of the mechanisms of MVG in control of shock boundary layer interaction.

Fig. 5.1 demonstrates the instantaneous numerical schlieren at the central plane. We can see many vortex rings appear in circular shapes. Informed with the prediction of vortex rings, the experimentalists in UT Arlington used some technology to validate the discovery. They used the particle image velocimetry (PIV) and the acetone vapor screen visualization to track the movement of the flow. More specifically, the flash of a laser sheet is used to provide the light exposure at a time interval of micro seconds. Fig. 5.2 presents a typical image at the center plane using PIV and the acetone vapor technology(Lu et al [47]). It is clearly demonstrated that a chain of vortex rings exists in the flow field after the MVG, same as shown in LES results (see Fig. 5.1).

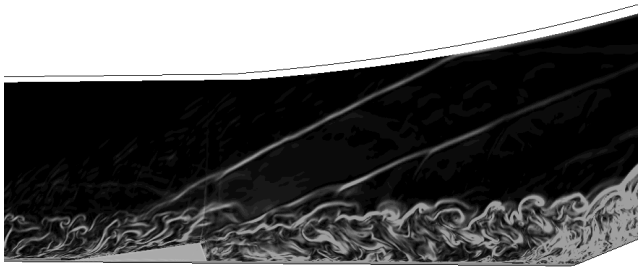

Figure 5.1 The Numerical Shilieren at the Center Plane

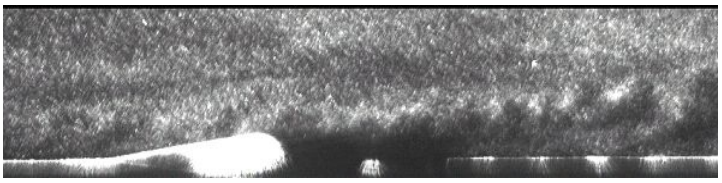

(a)

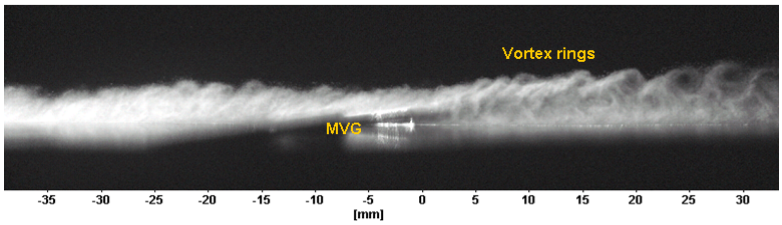

(b)

Figure 5.2 The Laser-sheet Flash Image at the Center Plane (Lu et al 2010) (a) Using PIV, (b) Using the Acetone Vapor

Our numerical discoveries of the vortex ring structures are also confirmed by 3-D PIV experiment (Fig. 5.3) conducted by Sun et al at Delft University [33]. Compared the two results, we can find the similar distribution of streamwise (ω_z) and spanwise vorticity (ω_x) components, which also proves the existence of ring structures. The Kevin-Helmholtz vortices part in Fig. 5.4 corresponds with the ring head in Fig. 4.28. The underneath part which is illustrated as streamwise vortices are two counter rotating primary vortices which are considered to be the main source of the ring structure as explained later .

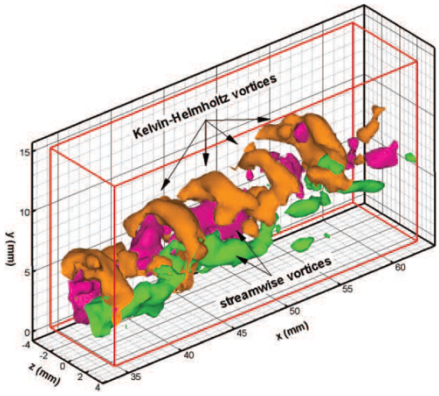

Figure 5.3 K-H rings behind MVG by (Sun et al 2011)

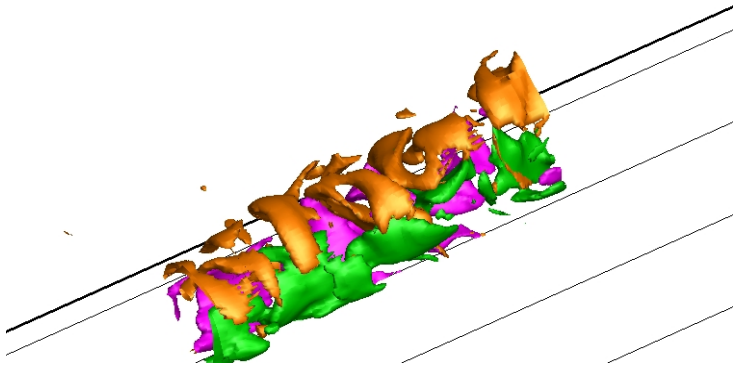

Figure 5.4 Distribution of Kelvin-Helmholtz Vortices and Streamwise Vortices from LES

The vorticity component which revolves towards the vertical direction (ω_y in our case) is not shown in Fig. 5.3 and 5.4. If this missing part was provided, we can see the vortex ring structure clearly by the combination of all the components of vorticity as shown in Fig. 5.5 which is in accordance with the structure in Fig. 4.28.

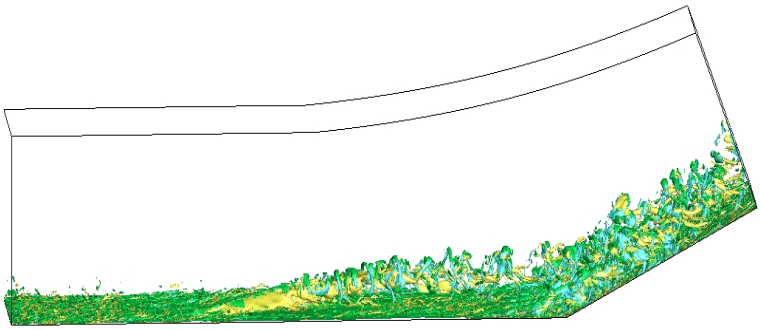

(a)

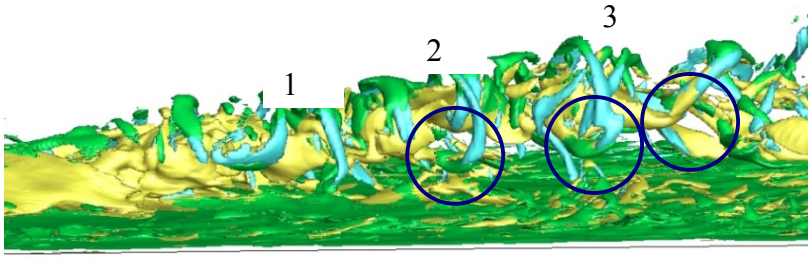

(b)

Figure 5.5 Vortex Rings shown by the Components of Vorticity (a) Global view (b) Close-up View

According to further analysis, we find that the ring structure is mainly composed by ω_x and ω_y while the streamwise vorticity component ω_z is absolutely the major source of two counter-rotating primary vortex inside the ring structure. ω_x constitutes the head and part of the bottom of the rings and ω_y forms the two sides. Also, the ring structure is not the perfect one since it is not closed on the bottom, instead, the two feet of each ring penetrate inside and connect with the inner primary vortices, as shown inside the circles in Fig. 5.5. In Fig. 5.6, the ring structure is clearly illustrated by both the total vorticity magnitude and each vorticity components. Actually, the vortex tube of each ring changes its direction and is connected to the two streamwise primary vorteics inside at the foot part which is clearlly shown in Fig. 15. Once the ring is generated, it will never break up into pieces or seperated parts and disconnect from the main vortex structure.

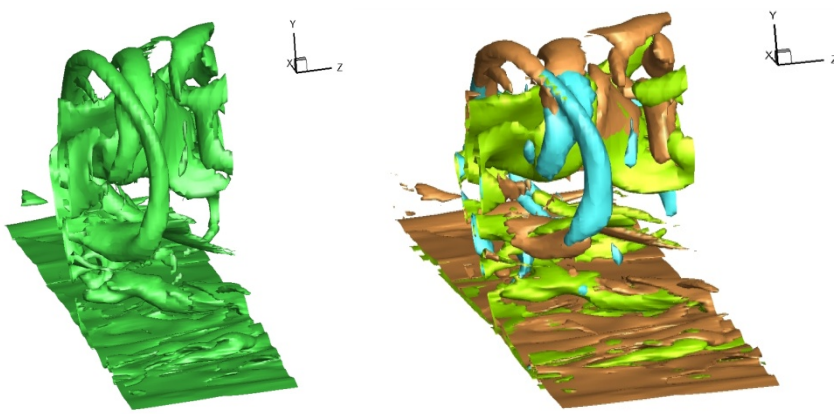

Figure 5.6 Part of the Ring Structure shown by Total Vorticity Magnitude (left) and each Components (right)

To further support the conclusion that the ring structure never breaks up and each ring has the feet connected inside, a close-up bottom view of vortex structure illustrated by λ_2 is given in Fig. 5.7 by another transient data set at different time and different location. Here, only half of the spanwise domain is used to make the vortex structure more clear. The iso-suface of

λ_2 can show the vortex tubes accurately and it captures two adjacent vortex rings in Fig. 5.7, and it apparently visualized the vortex tubes connect to the ring feet inside the vortex structure.

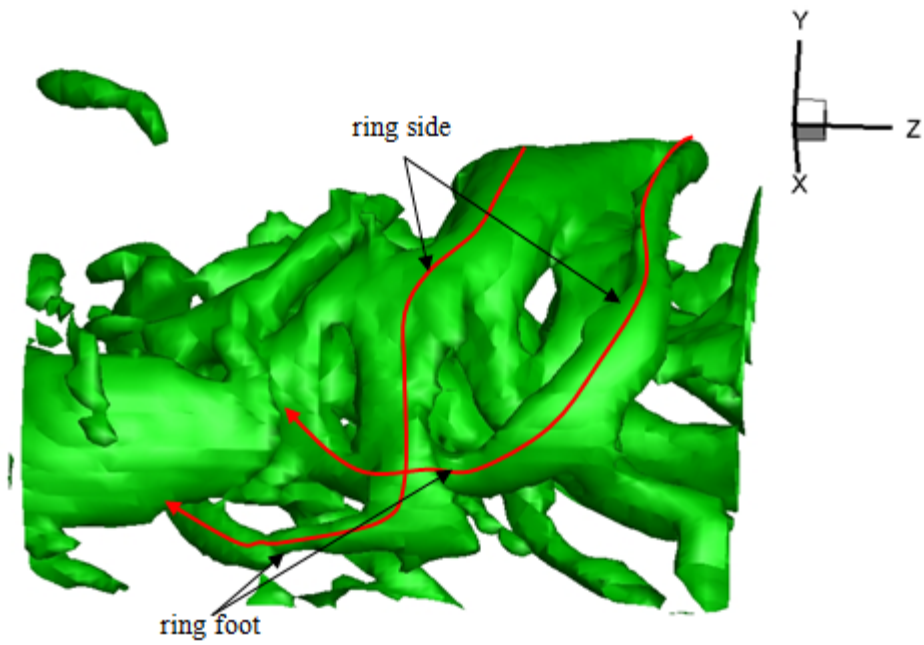

Figure 5.7 Part of the Ring Structure shown by λ_2(from the bottom view)

From the analysis of the magnitude of each vorticity component, ω_x and ω_z play the leading role during the process of propagating downstream. ω_x mainly origins from the shredding of the upstream MVG boundary layer, however, the other two components which forms the ring structure are separated from the viscous sub-layer underneath after about 1.1h away from the trailing edge of the MVG downstream. They are very likely following the vorticity conversion of the streamwise part. During the propagating, ω_x is reduced gradually and the rings are extended. In the end of the evolution, the momentum deficit (caused by streamwise vortex) disappears and the ring structure is totally distorted.

Fig. 5.8 shows the velocity field on a cross section in which it is found that the low speed flow from the viscous sub-layer is inhaled into the momentum deficit area continuously as

a result of two counter rotating streamwise vortices inside the rings. This may explain why the momentum deficit area can survive such a long way and determines the development of the ring structure. Fig. 5.9 is the flow field close to the foot and the head of a vortex ring which shows the vortex ring is extended outside by the velocity field around it, and that velocity field also helps the conversion between the components of vorticity.

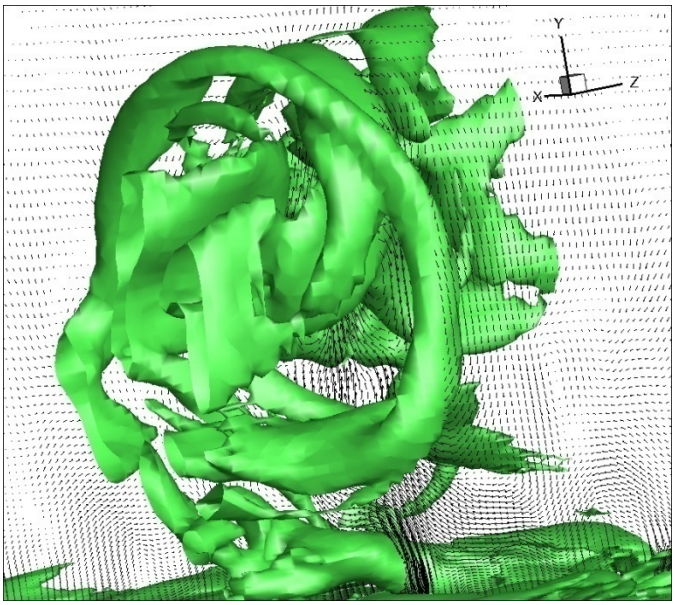

Figure 5.8 The Velocity Field on the Cross Section

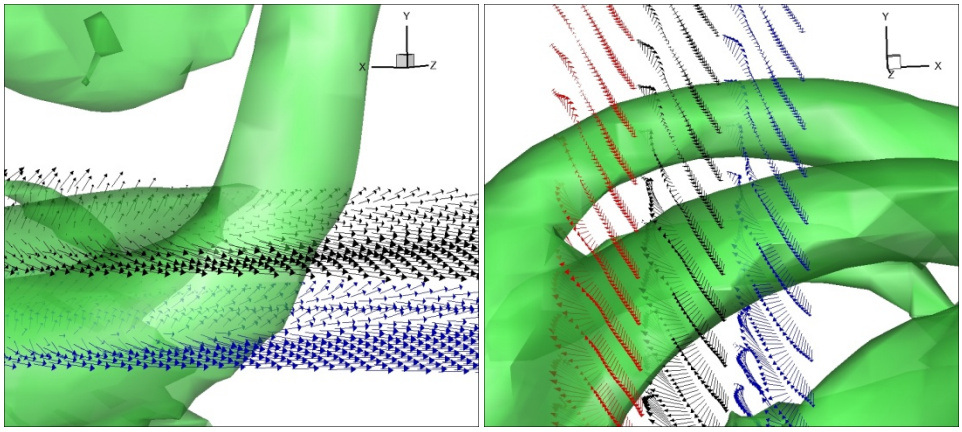

Figure 5.9 The Velocity Field close to the Foot (left) and the Head (right) of a Vortex Ring

5.2 Conservation of Vorticity

Because the original streamwise vortices and new generated vortex rings are both located away from viscous sub-layer for some distance, new vorticity in K-H vortex rings can only be transported to from the primary streamwise vortices if the distance is not far away from the MVG. The conservation of vorticity should make the vortices closely related to each other. The vorticity of the shear layer which results in the generation of the vortex rings should be transported from the original streamwise vortices. In order to investigate the relationship among the vortices, we measured the distribution of the maximum value of both streamwise and spanwise vorticity in a specific region (as seen in Fig. 5.10) to avoid the possible affection from the viscous sub-layer.

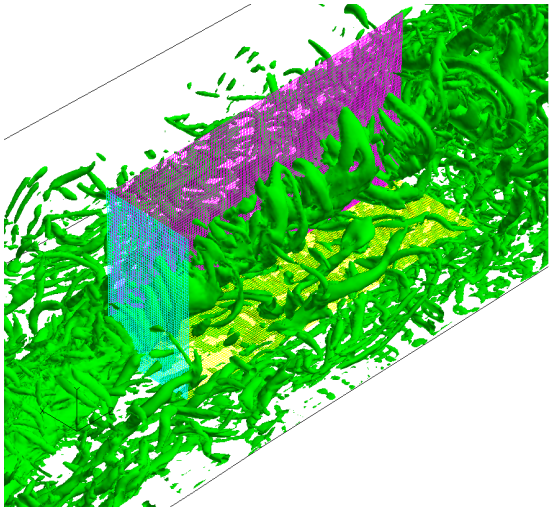

Figure 5.10 The Scope for Vorticity Magnitude Check

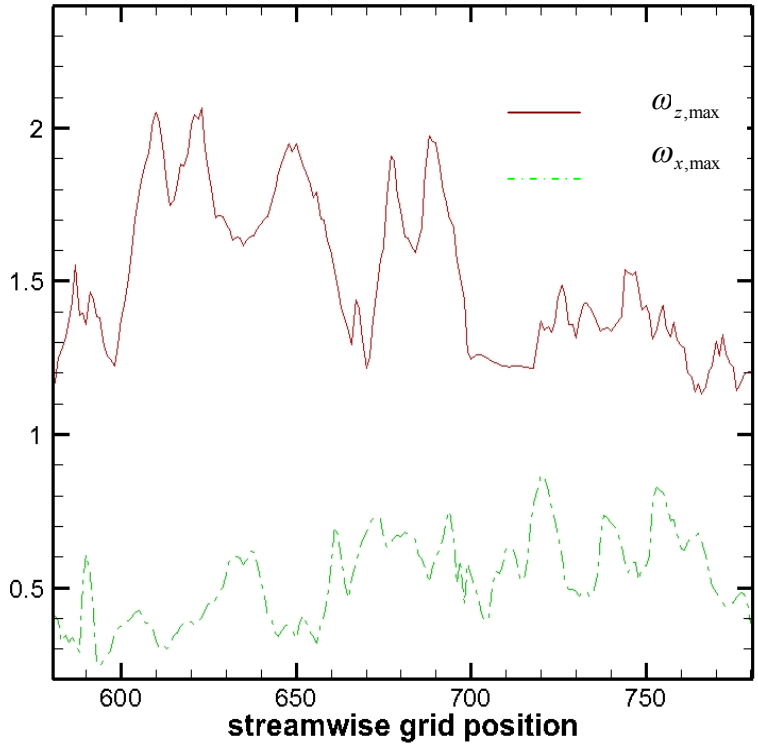

Figure 5.11 The Instantaneous Vorticity Distribution

Considering the pair of streamwise vortices are counter-rotating and vortex rings intersect the center plane in two locations, we only took the right half part and used positive values in Fig. 5.11. Since the grids are not uniform, it is more convenient to use streamwise grid position to mark the positions which range from about 1.0h to 9.5h after the trailing edge of MVG. Fig. 5.11 gives the instantaneous distribution of the two quantities along streamwise position of grids. From the figure and analysis of the flow field, the following results can be obtained:

1) The locations of the peaks of $\omega_{x,max}$ represent the upper intersection of the K-H vortex rings and the center plane. The positions of those peaks are nearly the same as the locations of the upper cores of new generated K-H vortex ring tubes which means the maximun value of spanwise vorticity happens on the ring head and at the central spanwise plane.

2) The quantities of $\omega_{x,max}$ and $\omega_{z,max}$ both substantially oscillate along the streamwise direction. The change of $\omega_{z,max}$ is relatively greater, while the quantity of the spanwise vorticity between the vortex rings appears relatively smaller. This is normal since the two counter rotating streamwise vortices are the main structure and almost only the streamwise vorticity is generated by MVG at very beginning.

3) There are two stages of the evolution of the vorticity, which reflect the interaction or coupling between the streamwise vorticity and vortex rings:

The first stage is the coupling stage from the beginning to about 700 ($z \approx 5h$ after the trailing edge of MVG). In this stage, not only the falling down of $\omega_{x,max}$ corresponds to the peaks of $\omega_{z,max}$, they also oscillate in the opposite directions. This is reasonable because in this period, the vortex rings, which are just generated, must obtain the vorticity from the primary streamwise vortex due to the vorticity conservation law.

The second stage, the post-coupling stage, starts from 700 to the end of box. In this stage, the momentum deficit area begins to disappear but the two curves still oscillate asynchronously. The interaction between streamwise and spanwise vorticity of course still exists, the quantity of the $\omega_{x,max}$ is reduced and the frequency of the oscillation is also increased. However, they are not directly against each other. This is because each new generated K-H vortex ring is stretching and developing individually. They are no longer aligned with the root on the vortex ring bottom.

The variation of the quantity of streamwise and spanwise vorticity confirms that vorticity of the rings comes from the streamwise votex structure inside the momentum deficit. Without enough complement of vorticity from the subviscous layer underneath, new generated spanwise vorticity can only be transported from the primary streamwise vorticity. Also, at the very beginning part of the first stage, when the vortex structure is not seperated from the subviscous layer absolutely, the variation of the two vorticity components keeps the same rule. This

declares that the conservation of vorticity plays the leading law during the whole process of the ring structure generation.

5.3 Stability Analysis to the Velocity Profile

In order to explore the mechanism of the vortex ring generation, the distributions of time and spanwise averaged streamwise-velocity are given in Fig. 5.12 along the normal grid lines at the central plane. The streamwise positions of the lines are $L_{from\ apex}/h \approx 3.3$, 6.7, 10 and 11, where $L_{from\ apex}$ is the streamwise distance measured from the apex of MVG. The dip of the lines corresponds to the momentum deficit. From the results, it can be seen clearly that there are at least two high shear layers in the central plane, one is located at the upper edge of the dip and the other is located at the lower edge. Within the shear layer, there is at least one inflection point. In order to demonstrate the existence of the inflection points, the second order derivative $\partial^2 w/\partial y^2$ (w is the streamwise velocity and y is the normal direction) is calculated along the lines, and the result of the line at $L_{from\ apex}/h \approx 3.3$ is plotted in Fig. 5.13 as an example. The existence and correspondence of the inflection points at the upper and lower shear layers is clearly illustrated as follow.

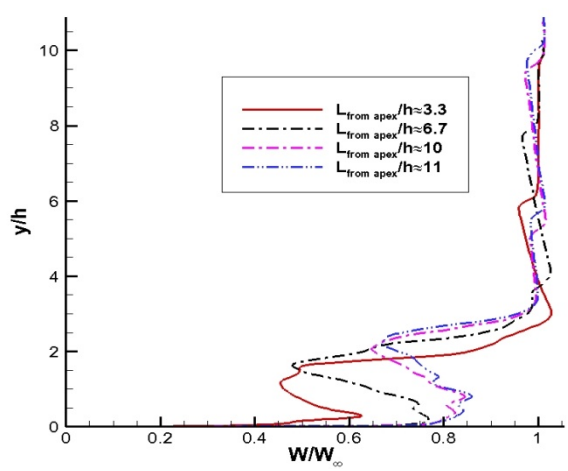

Figure 5.12 Averaged Streamwise Velocity at Different Sections

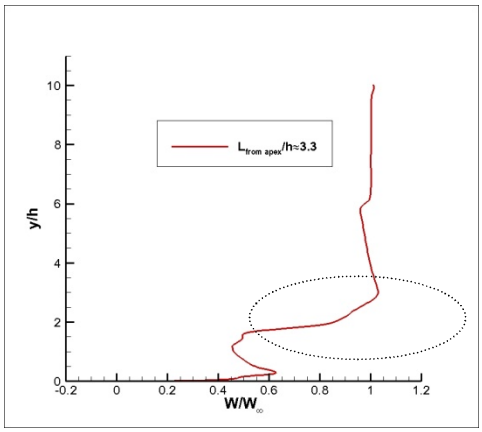

(a)

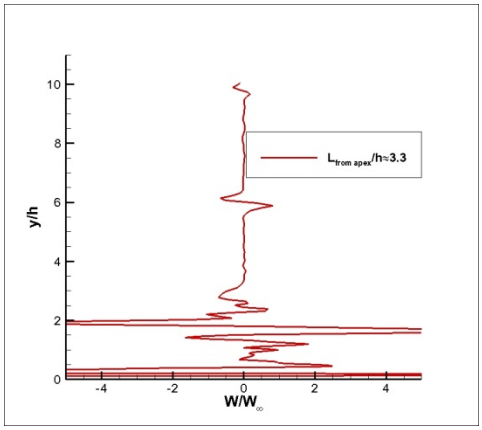

(b)

Figure 5.13 Inflection Points (surface for 3-D) (a) Averaged Streamwise Velocity at $_{Lfrom\ apex}$/h ≈3.3 (b) $\partial^2 w/\partial y^2$

It is obvious that the existence of the inflection point in shear layer will cause the flow losing the stability and generate vortex rollers by the Kelvin-Helmholtz instability (K-H) theory. So the mechanism for the vortex ring generation is a result caused by the K-H type instability, and the lost of the stability of the shear layer results in the roll-up of the vortex rings. In order to explore the mechanism of the vortex ring generation with viscous fluid, it is necessary to make analysis about stability upon the velocity profile.

5.3.1 Derivation of Linear Stability Equation

As discussed below, a linear stability analysis based on incompressible but viscous flow is conducted as following. First, the velocity profile of the upper boundary of the momentum deficit area (circled in Fig. 5.13a) is taken to study since the intensity of the upper shear layer appears to be stronger than that of the lower shear layer (Fig. 5.13a). If we can prove that, even for this temporal and spanwise averaged velocity profile, the flow is instable, and then the instantaneous velocity distribution should be unconditional instable.

$$\begin{cases} \dfrac{\partial V}{\partial t} + V \cdot \nabla V = -\nabla p + \dfrac{1}{\mathrm{Re}} \nabla^2 V \\ \nabla \cdot V = 0 \end{cases} \tag{5.1}$$

Equation (5.1) denotes the incompressible and non-dimensional Navier-Stokes equation in which, $V = (u, v, w)$ is the velocity vector. Considering that

$$q(x, y, t) = q_0(y) + q'(x, y, t) \tag{5.2}$$

where q can be specified as (u, v, w, p), $q_0 = (u_0, v_0, w_0, P_0)$ which indicates the value of mean flow, and q' denotes the corresponding linear perturbation. By eliminating the second order perturbation terms, the governing equation for small perturbations can be written as,

$$\begin{aligned} &\frac{\partial V'}{\partial t} + (V_0 \cdot \nabla)V' + (V' \cdot \nabla)V_0 + \nabla p' = \nabla^2 V' / \mathrm{Re} \\ &\nabla \cdot V' = 0 \end{aligned} \tag{5.2}$$

As a first step, a localized 2-D incompressible temporal stability for shear layer is conducted. Actually, it relates to the distance among two neighboring vortices in the central streamwise plane. Assume the normal mode is

$$\begin{aligned} V &= \hat{V}(y) e^{i(\alpha x + \beta z - \omega t)} + c.c. \\ p &= \hat{p}(y) e^{i(\alpha x + \beta z - \omega t)} + c.c. \end{aligned}, \tag{5.3}$$

where the parameter α is given, which is real and set to be 0.5 according to the averaged distance between the new generated rings, and c should be a complex number. By plugging in Equation (5.3), Equation (5.2) can be rewritten as,

$$\begin{aligned} L\hat{u} &= \mathrm{Re}(Du_0)\hat{v} + i\alpha\,\mathrm{Re}\,\hat{p} \\ L\hat{v} &= \mathrm{Re}(D\hat{p}) \\ L\hat{w} &= i\beta\,\mathrm{Re}\,\hat{p} \\ i(\alpha\hat{u} + \beta\hat{w}) + D\hat{v} &= 0 \end{aligned} \tag{5.4}$$

where $L = \{D^2 - (\alpha^2 + \beta^2) - i\,\mathrm{Re}(\alpha u_0 - \omega)\}$, and $D = \dfrac{d}{dr}$

Considering in 2D case (without *w*), and by eliminating $\hat{u}, \hat{p}$, we can obtain the standard O-S equation on $\hat{v}$,

$$(D^2 - \alpha^2)^2\hat{v} - i\alpha\,\mathrm{Re}[(U_0 - c)(D^2 - \alpha^2) - D^2U_0]\hat{v} = 0 \tag{5.5}$$

Equation (5.5) is about $\hat{v}$, but we need to get the value of *c*. The value of *c* determines the property of stability of the equation. Let $c = c_r + ic_i$, if $c_i > 0$, then the disturbance will continuously grow and the flow would be instable. Otherwise, the flow would be stable.

5.3.2 Stability Analysis to the Averaged Velocity Profile

If there is no disturbance at the boundary and it will be free stream outside the domain (*a, b*), then we have the corresponding boundary condition for function $\hat{v}$ as $\hat{v}(a) = \hat{v}(b) = 0$ and $D\hat{v}(a) = D\hat{v}(b) = 0$. The second order central difference scheme (Equation (5.6)) is used to derive the finite different equation from Equation (5.4),

$$\begin{cases} D^2\psi = (\psi_{n+1} - 2\psi_n + \psi_{n-1})/h^2 \\ D^4\psi = (\psi_{n+2} - 4\psi_{n+1} + 6\psi_n - 4\psi_{n-1} + \psi_{n-2})/h^2 \end{cases} \tag{5.6}$$

Apply (5.6) to Equation (5.5) we can get the generalized eigenvalue problem:

$$A\varphi + Bc\varphi = 0 \tag{5.7}$$

Where A (symmetric pentadiagonal matrix) and B (symmetric tridiagonal matrix) are the coefficients' matrix and the vector φ denotes the values of $\hat{v}$ at different position. *c* becomes the generalized eigenvalue of Equation (5.7).

$$A=\begin{bmatrix} a_{11} & a_{12} & a_{13} & 0 & . & . & . & . \\ a_{21} & a_{22} & a_{23} & a_{24} & 0 & . & . & . \\ a_{31} & a_{32} & a_{33} & a_{34} & a_{35} & 0 & . & . \\ . & . & . & . & . & . & . & . \\ . & . & . & . & . & . & . & . \\ . & . & . & 0 & a_{n-2,n-3} & a_{n-2,n-2} & a_{n-2,n-1} & a_{n-2,n} \\ & & & & 0 & a_{n-1,n-2} & a_{n-1,n-1} & a_{n-1,n} \\ & & & & & 0 & a_{n,n-1} & a_{n,n} \end{bmatrix} \tag{5.8}$$

$$B=\begin{bmatrix} b_{11} & b_{12} & 0 & 0 & . & . & . & . \\ b_{21} & b_{22} & b_{23} & 0 & 0 & . & . & . \\ 0 & b_{32} & b_{33} & b_{34} & 0 & 0 & . & . \\ . & . & . & . & . & . & . & . \\ . & . & . & . & . & . & . & . \\ . & . & . & 0 & b_{n-2,n-3} & b_{n-2,n-2} & b_{n-2,n-1} & 0 \\ & & & & 0 & b_{n-1,n-2} & b_{n-1,n-1} & b_{n-1,n} \\ & & & & & 0 & b_{n,n-1} & b_{n,n} \end{bmatrix} \tag{5.9}$$

$$\varphi = (\varphi_1, ..., \varphi_n)^t \tag{5.10}$$

In the mth line of matrix A and B,

$$a_{m+2} = 1/h^4 \tag{5.11}$$

$$a_{m+1} = -4/h^4 - (2\alpha^2 + i\alpha \operatorname{Re} U_0)/h^2 \tag{5.12}$$

$$a_m = 6/h^4 + (4\alpha^2 + 2i\alpha \operatorname{Re} U_0)/h^2 + \alpha^4 + i\alpha \operatorname{Re}(\alpha^2 + D^2 U_0) \tag{5.13}$$

$$a_{m-1} = -4/h^4 - (2\alpha^2 + i\alpha \operatorname{Re} U_0)/h^2 \tag{5.14}$$

$$a_{m-2} = 1/h^4 \tag{5.15}$$

$$b_{m+1} = \frac{i\alpha \operatorname{Re}}{h^2} \tag{5.16}$$

$$b_m = \frac{2i\alpha \operatorname{Re}}{h^2} \tag{5.17}$$

$$b_{m-1} = \frac{i\alpha \operatorname{Re}}{h^2} \tag{5.18}$$

By solving the general eigenvalue problem (5.7), we can get the physical solution of the frequency *c*, whose imaginary part c_i is about 0.068 for our case. The positive value means this kind of flow is unstable. Fig. 5.14 shows the corresponding shape of the eigenvector function, $\hat{v}$.

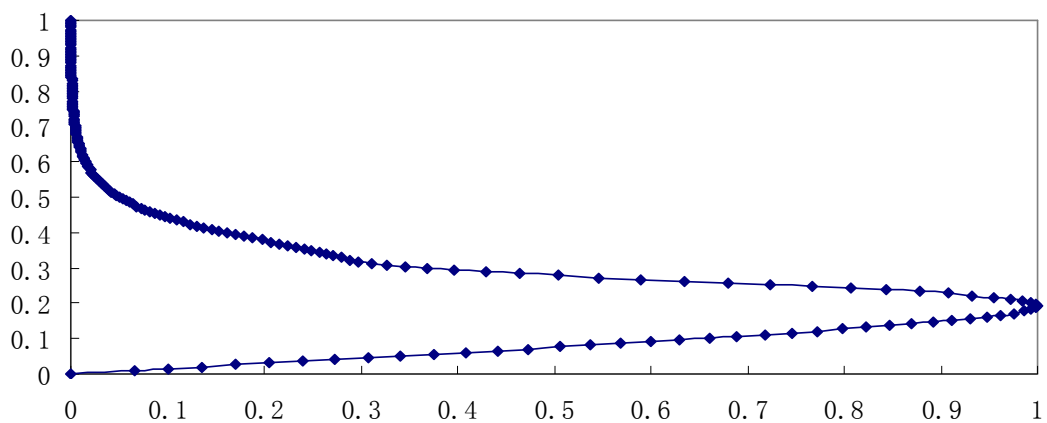

Figure 5.14 Eigenvector Function of $\hat{v}$

The lost of the stability of the shear layer will result in the roll-up of the vortex, which appears in ring-like structure in a 3-D view. In Fig. 5.15, the 3D distribution of three components of vorticity is given right after the MVG. It shows that spanwise vorticity is first generated at the top of momentum deficit area where clusters the streamwise vortices. After that, the ring sides for the first ring are also generated on the boundary of momentum deficit. This confirms our assumption above. The top boundary of the momentum deficit has the most instable shear

layer, so the spanwise vorticity is first generated while the corresponding vortex directly connect to the streamwise vortex inside at first. Then the rings show up soon due to the evolution of the instable shear layer. Also we can find that the whole ring is generated on the boundary of the momentum deficit, neither from inside nor outside region. So, the shear layer instability is the main mechanism of the ring generation.

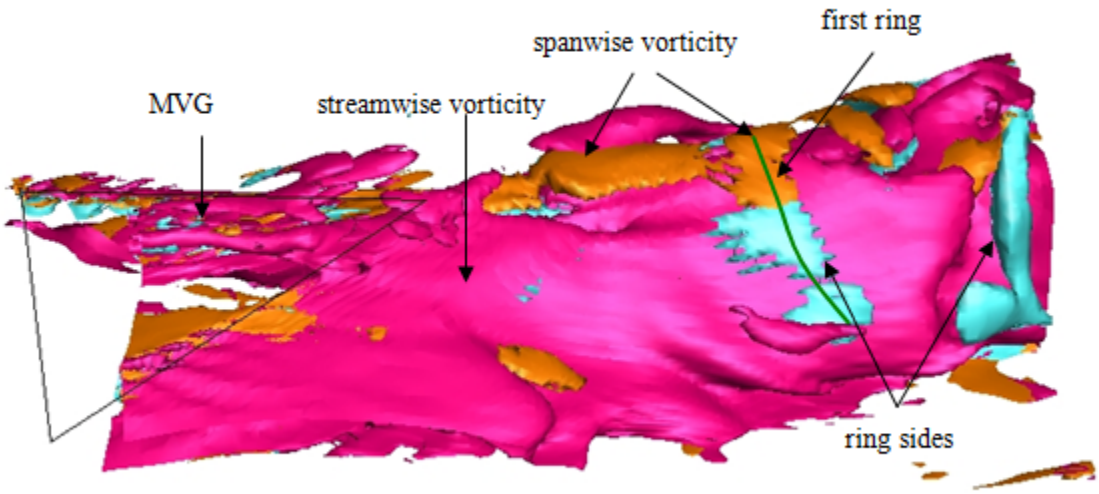

Figure 5.15 The Instantaneous Vorticity Distribution

The mechanism of the ring generation is a real 3D process. Study in non-linear, 3D and compressible stability analysis is needed to reveal the full mechanism of the shear layer instability behind MVG. The current study only involves temporal, linear, and incompressible stability analysis which can be considered as a first step to study the wake instability of MVG.

The interaction between the streamwise vortices and vortex rings shown by vorticity is a new interesting phenomenon. The interaction and vorticity conservation of the primary streamwise vortex and new generated K-H vortex ring needs validation by experiment and the mechanism is still under investigation.

CHAPTER 6

NUMERICAL STUDY ON SHOCK WAVE-VORTEX RING INTERACTION

The new generated vortex ring discussed above will immediately interact with the shock wave induced by the ramp part. Vortex-shock wave interaction [59] has been studied a lot. Main concerned issues in this topic are: a) the deformation of the shock wave; b) the multistage features of the interaction caused by the vortex interacting with the primary shock and the reflection shocks, etc; c) the acoustic characteristics, which includes near- and far-field of acoustic, the dipole and quadruple acoustic pressure structure, etc.

Compared with the classic study Ref. 60-62, the vortex rings-shock interaction of the MVG controlled ramp flow is different case and could bring a new topic. The differences are: a) the interaction is a more complicated 3-D one than the 2-D counterpart, which happens between 3-D vortex rings and the oblique shock wave; b) the interaction happens within or close to the boundary layer and the separation region, where other flow structures exist like vortices with small scale besides the shock wave; c) the interaction is a continuous one, not a one-time event; d) besides the rings, components of the primary vortices still exist and make the interaction more complicated. Although differences are obvious, results obtained in the standard vortex ring-shock interaction can still give hints and suggestions to the current research.

6.1 Influence on Ring Structure by the Interaction

In order to make further analyses, it is necessary to get the kinetic information of the vortex rings. According to the results of computation, it is found that vortex rings appear irregularly after the MVG and before the ramp. They are continuously distorted during propagating. Thus, only 3 of these rings (marked in Fig. 5.5b) are checked since they are

relatively regular at this stage. It shows that they almost propagate in the same speed and the averaged parameters are presented in table 6.1.

Table 6.1 Characteristic Parameters of Vortex Rings on the Plate

Δs_{ring}	$V_{ring,1}$	T_{ring} (h/U_∞)	St_h
1.21h	$0.78U_\infty$	1.55	0.26

The shape of vortex rings is badly deformed before they penetrate the shock wave and travel along the ramp. But it is still possible to obtain the rough speed of the two obvious vortex rings right in front of and behind the shock (see Fig. 6.1, marked as 1 and 2), the value of the streamwise velocity can be found as: $V_{ring,1} \approx 0.77U_\infty$, $V_{ring,2} \approx 0.47U_\infty$

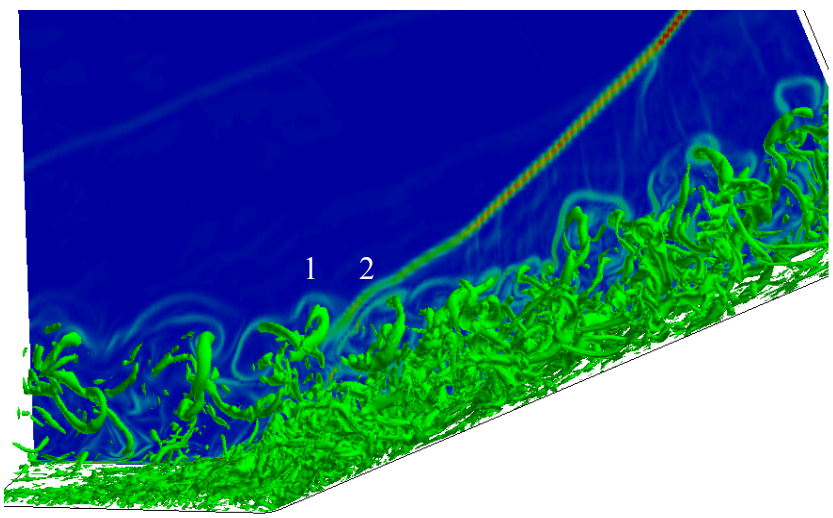

Figure 6.1 The Three Vortex Rings above the Ramp for Measurement

For the second ring, $V_{ring,2}$ is only the streamwise velocity, it will become about $0.68U_\infty$ while evaluated along the direction of ramp. The value is in consistency with the known knowledge, i.e., typical convective structures usually travel at a speed around $0.7U_\infty$. For the first velocity $V_{ring,1}$, the result has the same quantity level as well. We can also find that the total

speed of the ring dose not change much when it penetrates the shock wave. The little decrease to the velocity may be caused by the interaction between ring and viscous sub-layer since the rings merge into the lower layer in the boundary layer after they penetrate the shock. However, this phenomenon needs to be further verified.

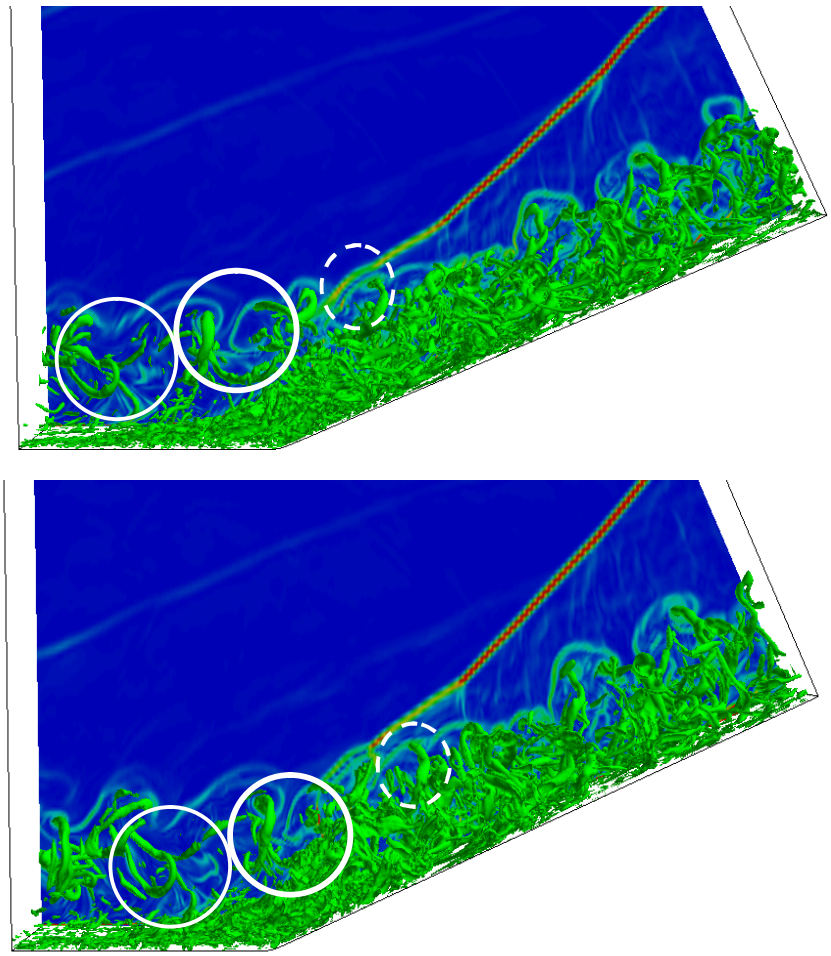

Figure 6.2 The 3D View of the Propagating Rings at the Ramp part at Different Time

In Fig. 6.2, we tracked 3 different rings when they are moving. When the vortex ring is passing through the shock wave, the vortex structure is slightly distorted but not damaged; the vortex ring does not break down by penetrating the strong shock wave and even keeps the topology very well. Since the vortex ring is distorted continuously after it is created (as we can

find in Fig. 6.2, the first ring in circle), there's no conclusion that the interaction of vortex rings and shock makes the ring to be distorted. The distortion of rings could be induced by the particular flow field of inside and outside the ring structure, or the compressing effect of the ramp. In Fig. 6.2 and Fig. 6.3 we can also find that those vortex rings exist after penetrating the shock wave and their topology are well maintained to the end of the ramp. That means in this 3D case, shock rarely affects the vortex structure. Fig. 6.4 shows the streamwise vorticity distribution at the central plane right before and after a vortex ring penetrates the shock wave, from which we can find that the shock rarely determines the evolution of the vortex rings at the head part and the vorticity distribution is not changed much. Those rings pass the shock wave rather smoothly.

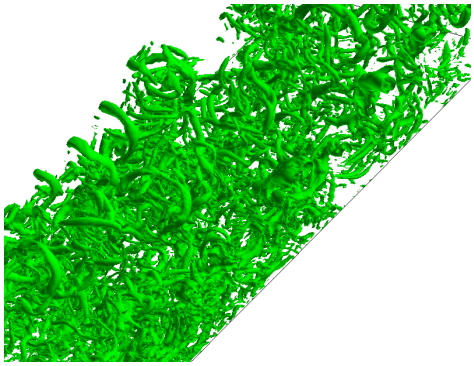

Figure 6.3 The Ring Structure at the Ramp part by λ_2

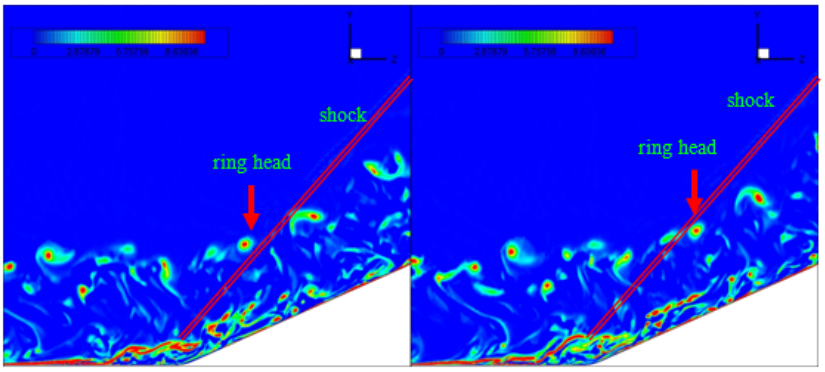

Figure 6.4 Streamwise Vorticity Distribution at two Different Time Steps

The interaction of vortex rings and shock wave can be explained with Richtmyer-Meshkov instability (RMI) to some extent. It occurs when an interface between fluids of differing density is impulsively accelerated, e.g. by the passage of a shock wave. The vortex rings structure is a wave of differing densities, the process of passing the shock wave is the same with that in RMI theory. The key point of RMI is the baroclinic effection between $\nabla\rho$ and ∇p.

$$\frac{d\Omega}{dt} - (\Omega \cdot \nabla)\mathbf{v} + \Omega(\nabla \cdot \mathbf{v}) = \nabla \times \mathbf{F} + \frac{1}{\rho^2}\nabla\rho \times \nabla p + \nabla \times (\nu\Delta\mathbf{v}) + \frac{1}{3}\nabla \times (\nu\nabla(\nabla \cdot \mathbf{v})) \quad (6.1)$$

The quantity of $|\nabla\rho \times \nabla p|$ plays a very important role to the vorticity disturbance. Actually, it is the most important source term in the process of vorticity variation (Equation (6.1), where Ω denotes the vector of vorticity, F is the external volume force) in our case. Fig. 6.5 shows the iso-surface of $|\nabla\rho \times \nabla p|$ with different values, we can find that : a) The greater value of $|\nabla\rho \times \nabla p|$ only exists in a small area, thus the flow field, especially the vortex structure is rarely affected. b) The small value of $|\nabla\rho \times \nabla p|$ mainly happens in the bottom of the boundary layer, so the shock wave will not change the vortex rings a lot while those rings only exist on the upper side of the boundary layer. That is the reason for why the ring structure is so robust and never break down even when it penetrates the strong shock wave.

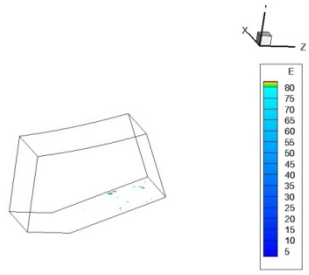

(a)

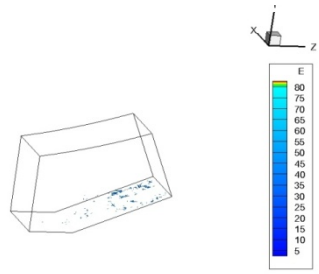

(b)

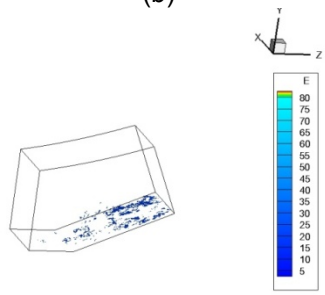

(c)

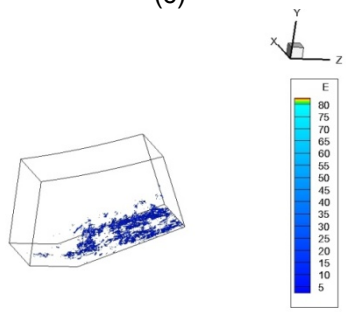

(d)

Figure 6.5 Iso-surface of $|\nabla\rho\times\nabla p|$ in the Ramp Part (a) $|\nabla\rho\times\nabla p|=80$ (b) $|\nabla\rho\times\nabla p|=40$ (c) $|\nabla\rho\times\nabla p|=20$ (d) $|\nabla\rho\times\nabla p|=10$

From all discussed above, we can conclude that the interaction with strong shock wave dose not influence the ring structure much. Those rings keep their shapes, the quantity of vorticity, and also travel normally like the shock is missing. However, after penetrating the shock wave, the quantity of density and pressure gradient seems increased in the ring structure as seen in Fig. 6.6. This phenomenon needs to be further studied.

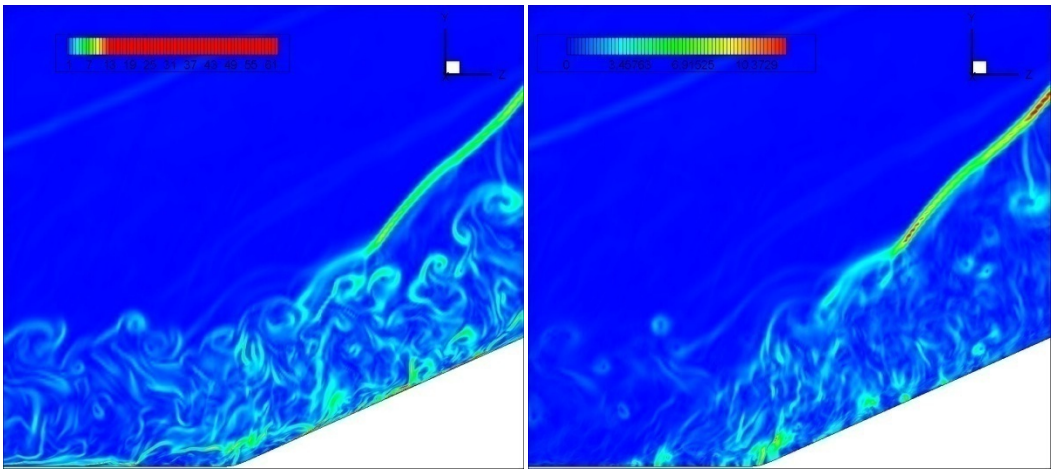

Figure 6.6 Density Gradients (left) and Pressure Gradient (right) on the Central Plane

6.2 Influence on Oblique Shock Wave

As newly found structure, the string of vortex rings are fully 3D structures. Thus the interaction with shock wave have different features from classic 2-D ones.

To better illustrate the process, two kinds of sections are investigated: the centre plane and then a series of spanwise computational planes with constant streamwise index. In Fig. 6.7, the gradient fields of density $|\nabla\rho|$ and pressure $|\nabla p|$ at two different moments are employed to analyze the interaction. Fig. 6.8 gives the contour of $|\nabla\rho|$ and $|\nabla p|$ of spanwise computational planes at the same three successive moments. In order to get the overall understanding of the interaction, it is also necessary to directly give the 3-D shape of the shock wave. In Fig. 6.9, six snapshots are obtained using the iso-value of pressure. The value of pressure is selected to

make the inner shock layer be exposed and seen from outside. The shape of the strong shock wave is given by $|\nabla p|$ in Fig 6.10.

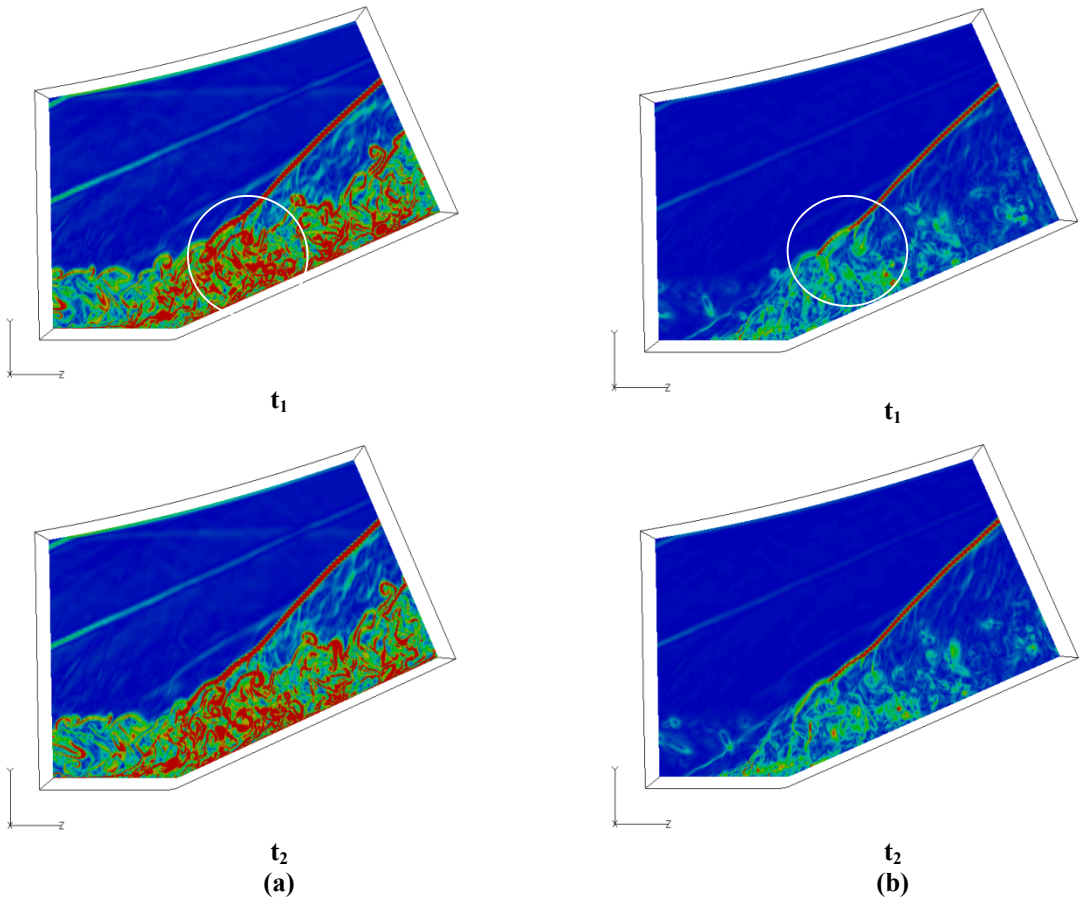

Figure 6.7 Contours of a) $|\nabla \rho|$ and (b) $|\nabla p|$ at Two Moments at the Center Planes

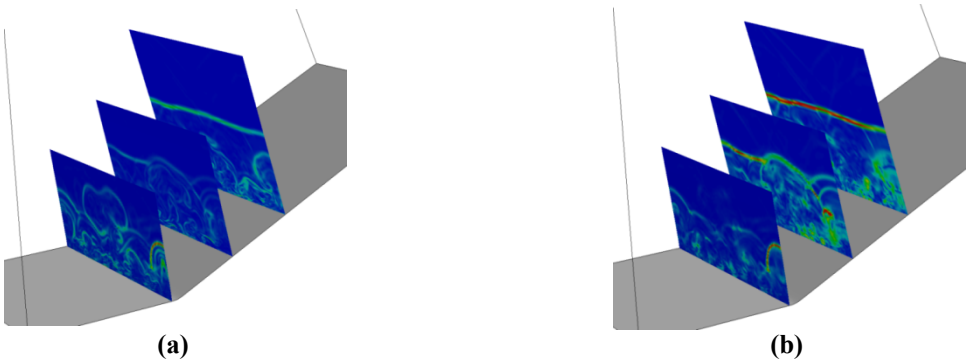

Figure 6.8 The Contours of (a) $|\nabla \rho|$ and (b) $|\nabla p|$ at Spanwise Sections and at Four Successive Moments

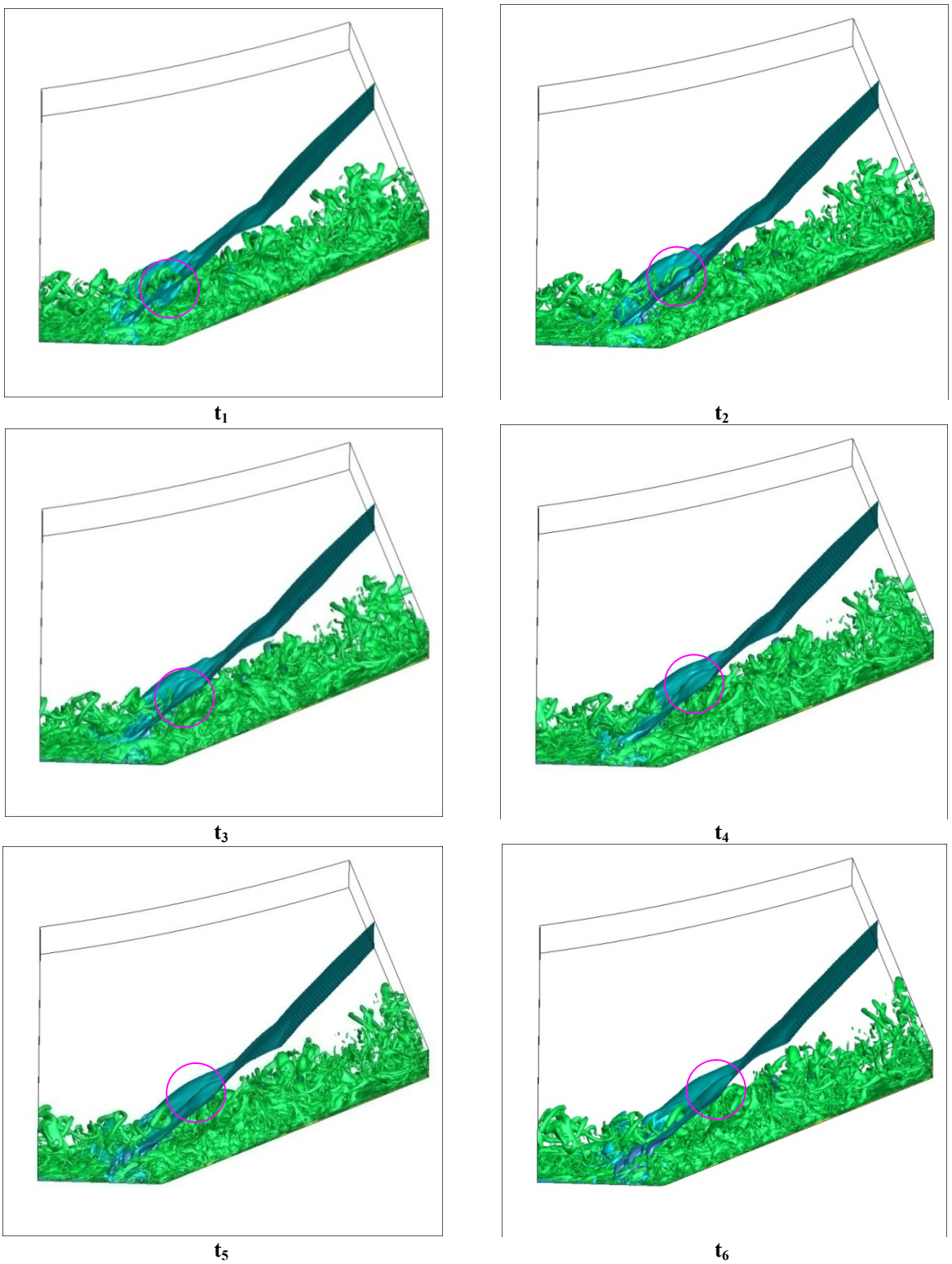

Figure 6.9 The Shock Wave Shape by the Iso-surface of Pressure and Ring Structure by λ_2

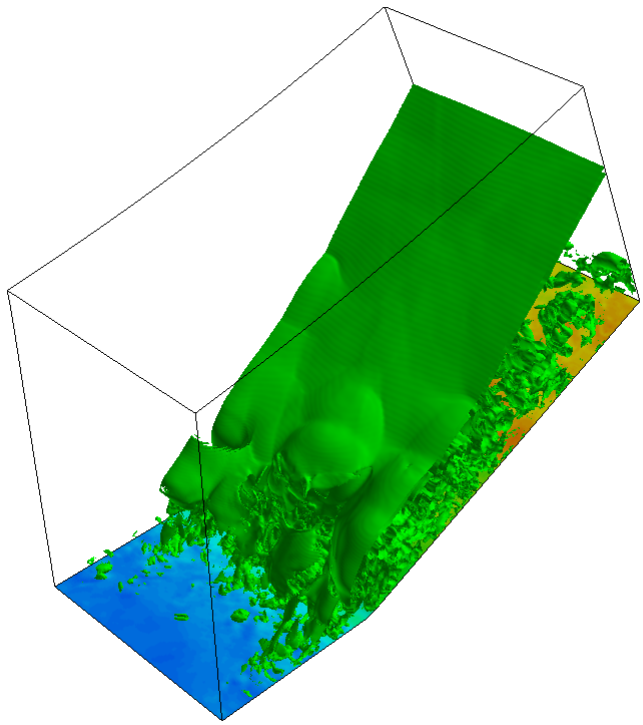

Figure 6.10 The 3D Shock Wave Shape by $|\nabla p|$

From the figures, the following features can be observed:

1) In Fig. 6.7, it demonstrates that there are at two layers of shock wave or wave structures after the corner: upper one is the original but quite weaker separation/reflection shock; the other is the stronger interacting shock wave caused by the vortex rings. These two layers of shocks will merge into one shock wave afterwards, i.e., the oblique shock caused by ramp.

2) Comparing Fig. 6.7(a) and (b), it can be found that there is a slip line under the curved shock in the contour of $|\nabla \rho|$, which cannot be found in the contour of $|\nabla p|$. The slip line indicates the density change across the line, while the pressure keeps the same at the both sides of the line. After checking the movie about $|\nabla \rho|$, the slip line comes from the original connections between vortex rings.

3) In Fig. 6.8 we can found that when a vortex ring penetrates into the shock wave, the interaction part of the shock is distorted and its intensity is also reduced a lot.

4) In Fig. 6.9, 6.10, it shows that the interaction between shock wave and vortex rings is in fully 3D. The flow field lost its symmetry and it can be clearly illustrated by the shape of shock wave. Multilayer structures and the bump like 3-D shape is one of the typical characteristics of the shock-vortex interaction.

5) In Fig. 6.10 it can be observed that, at the corner of the ramp, there is no obvious sign of shock waves, and the original shock wave retreats to a downstream position on the ramp. This result shows that the separation/reflection shock wave is eliminated near the corner. We can see that it is induced by the interaction with vortex rings and the viscous sub-layer (Fig. 6.9). This kind of phenomenon is a complicated turbulence-shock wave interaction which should be studied further.

6) When the vortex rings pass through the shock wave (Fig. 6.9 at time t_1), the shock wave will be distorted like a bump (Fig. 6.9 at time t_3), and the bump will be gradually smoothed when propagating downstream. We can clearly see that this shape is caused by the vortex ring-shock wave interaction. When the vortex enters the shock wave and moves away from it, the distortion subsides quickly. The subsequent incoming vortices will repeat the process. At the fifth section in Fig. 6.9, the bump shape is less observable, which indicates the vortex combination moves far below the shock wave and have less influence on the separation/reflection shock wave.

To explain the mechanism of the bump shape of the 3D shock wave, in Fig. 6.11, the second ring in Fig. 6.1 (marked as 2) is taken out and the flow filed on a spanwise cross section which passes through the center of this ring is plotted. The velocity field is the tangent projection of the 3D velocity vector distribution on the cross section which ignores the velocity component along the ramp direction. The projection of free stream velocity moves towards the ramp since the cross section is vertical to the ramp surface. Meanwhile, as noticed in Fig. 6.1, when the vortex rings enter the shock wave, they incline to some degree to the ramp. What is very

interesting is that the vector field shown in the section clearly demonstrates the upward induction of the flow at the center position of the ring. The inducted flow will interact with the incoming free stream and make the surface of the interaction which is the location of the shock wave to be an obvious arc-like boundary.

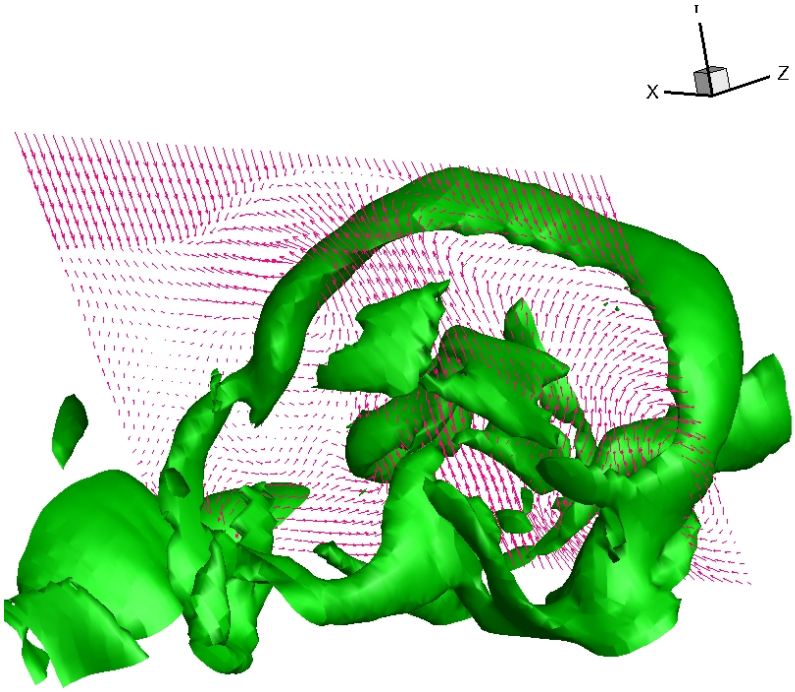

Figure 6.11 The Vector Field at a Spanwise Section with Vortex Structure shown by Total Vorticity

However, the interaction between the vortex ring structure and shock wave is a new interesting phenomenon. The existence of the interaction needs the verification of experiment, and the mechanism is still under discussion.

CHAPTER 7

CONCLUDING REMARKS

In this work, by using the implicitly implemented large eddy simulation method with fifth order bandwidth-optimized WENO scheme, comparative studies are made on the MVG-ramp flow and the ramp flow without MVG at M=2.5 and Re_θ=5760. A body-fitted grid scheme is adopted to make the computational accuracy as high as possible.

Through the computation on the ramp flow, the basic structures of the flow field are captured by the simulation such as the separation shock wave by the SBLI, instantaneous small scale vortices in the separation zone, stripe structure, etc. Statistics are made by taking time average to the flow field. Large scale streamwise vortices are found in the sense of averaging. The results can be used for comparison with those in the MVG-ramp flow.

Through the computation on the MVG-ramp flow, the same basic wave system is obtained as that given by Babinsky. Reasonable agreement in the shape of shocks between the computation and experiment is obtained. The subtle oblique "λ" structure of the re-compression shock wave is found in computation as well, which indicates the resolution in computation is high.

The comparison between the MVG-ramp flow and the ramp flow without MVG shows that, the MVG can distinctly reduce the separation zone and improve the shape factor. One possible disadvantage of MVG is that it may lower the value of the Pitot pressure recovery coefficient.

A number of new findings and new mechanisms are obtained through the LES simulation because of the high order accuracy and high resolution of the computation, which include:

i). The complete separation topology is obtained, a representative pair of spiral points are found on the plate beside the end of MVG, which implies a new five-pair-vortex model around the MVG, and the model is different from the one reported by previous literatures.

ii). The mechanism of the formation of the momentum deficit is investigated. It is found that the deficit mainly comes from the shedding of the upstream boundary layer, which is entrained by the streamwise vortices to form the circular structure.

iii). The structures of the surface pressure are described, and the 3-D structures of the re-compression shock waves are presented. Especially, the head and leg of the re-compression shock waves are found to be separated in the initial stage but connected afterwards, and therefore the shock wave becomes arc shaped therefore. The connection between the shock waves, the flow structures and separations is discussed and obtained.

iv). A new phenomenon and its mechanism are discovered in MVG-ramp flow control, i.e., the vortex rings generated by the high shear layer. Vortex rings are generated and strongly interact with the separation zone and the separation shock, and play an important role in the reduction of the size of the separation zone.

Base on numerical results, the vortex ring structure is studied in detail. The inflection points inside the momentum deficit area are found. The mechanism for the vortex rings was analyzed and found that, the existence of the high shear layer and inflection surface generated by the momentum deficit will cause the corresponding Kelvin-Helmholtz instability, which develops into a series of vortex rings. The interaction between vortex ring structure and the oblique shock by the MVG controlled ramp flow is also studied. It shows that the ring structure does not break down and keeps it topology after penetrating the strong shock wave, while the strong oblique shock is influenced a lot by the induced flow field from vortex rings. The mechanism during the interaction is also discussed.

REFERENCES

[1] Lin J. C. *Review of Research on Low-Profile Vortex Generators to Control Boundary-Layer Separation*. Progress in Aerospace Sciences, Vol. 38, pp.389-420(2002).

[2] Ashill, P. R., Fulker, J. L., Hackett, K. C. *A Review of Recent Developments in Flow Control*. The Aeronautical Journal, 109, 1095, pp.205-232(2005).

[3] Anderson, B. H., Tinapple, J. Surber, L. *Optimal Control of Shock Wave Turbulent Boundary Layer Interaction Using Micro-Array Actuation*. AIAA paper 2006-3197.

[4] Hoden, H. A., Babinsky, H. *Vortex Generators Near Shock/Boundary Layer Interactions.* AIAA paper 2004-1242.

[5] Ford, C. W., P,, Babinsky,H. *Micro-Ramp Control for Oblique Shock Wave/Boundary Layer Interaction.* AIAA paper 2007-4115.

[6] Holden, H.,Babinsky. *Effect of Microvortex Generators on Separated Normal Shock/Boundary Layer Interactions.* AIAA J.pp.170-173(2007).

[7] Babinsky, H., Li, Y., Ford, C. W. P. *Microramp Control of Supersonic Oblique Shock-Wave/Boundary-Layer Interactions.* AIAA J., Vol. 47, No. 3, pp.668-675(2009).

[8] Ghosh, S., Choi J., Edwards, J. R. *RANS and Hybrid LES/RANS Simulations of the Effects of Micro Vortex Generators Using Immersed Boundary Methods*. AIAA paper 2008-3726.

[9] Lee, S. Loth E. , Wang, C. *LES of Supersonic Turbulent Boundary Layers with μVG's.* AIAA Paper 2007-3916.

[10] Lee, S., Loth, E. *Supersonic Boundary Layer Interactions with Various Micro-Vortex Generator Geometries.* AIAA Paper 2009-3712.

[11] Dolling, D. S., Murthy, M. *Unsteadiness of the Separation Shock Wave Structure in a Supersonic Compression Ramp Flowfield.* AIAA J., Vol. 12, pp.1628-1634(1983).

[12] Dolling, D. S. *High-Speed Turbulent Separated Flows: Consistency of Mathematic Models and Flow Physics.* AIAA J., Vol. 36,pp. 725-732(1998).

[13] Dolling, D. S. *Fifty Years of Shock-Wave/Boundary-Layer Interaction Research: What next?* AIAA J., Vol. 39, pp. 1517-1531(2001).

[14] Settles, G. S. Dodson, L. J. *Supersonic and Hypersonic Shock/Boundary Layer Interaction Database.* AIAA J., Vol. 32, 1377-1383(1994).

[15] Dussauge, J. P., Dupont, P., Debieve, J. F. *Unsteadiness in Shock Wave Boundary Layer Interaction with Separation.* Aerospace Science and Technology, Vol. 10, No. 2, pp.85-91(2006).

[16] Andreopoulos, J., Agui, J. H., Briassulis, G. *Shock Wave-Turbulence Interactions,* Annu. Rev. Fluid Mech., Vol. 32, pp.309-345(2000).

[17] Loginov, M. S., Adams, N. A., Zheltovodov, A. A. *Large-Eddy Eimulation of Shock-Wave/Turbulent-Boundary-Layer Interaction.* J. Fluid Mech., Vol. 565, pp. 135-169(2006).

[18] Wilcox, D., *Turbulence Modeling for CFD*, DCW Industries, Inc., 1993

[19] Zheltovodov, A. A. *Advances and Problems in Modeling of Shock Wave Turbulent Boundary Layer Interactions.* Proceedings of the international Conference on the Methods of Aerophysical research, Institute of Theoretical and Applied Mechanics, Novosibirsk, Russia, pp.149-157(2004)

[20] Rizzetta, D., Visbal, M. *Large Eddy Simulation of Supersonic Compression-Ramp Flow by High-Order Method.* AIAA J., Vol. 39, No. 12, pp.2283-2292(2001).

[21] Kaenel, R.V, Kleiser, L. Adams, N. A. Vos, J. B. *Large-Eddy Simulation of Shock-Turbulence Interaction.* AIAA J., Vol. 42, No. 12, pp.2516-2528(2004).

[22] Adams, N. A. *Direct simulation of the turbulent boundary layer along a compression ramp at M = 3 and Reθ = 1685.* J. Fluid Mech., Vol. 420, pp. 47-83(2000).

[23] Wu M. Martin, M. P. *Direct Numerical Simulation of Supersonic Turbulent Boundary Layer over a Compression Ramp*. AIAA J., Vol. 45, No. 4(2007).

[24] Martín, M. P. *Direct Numerical Simulation of Hypersonic Turbulent Boundary Layers. Part 1. Initialization and Comparison with Experiments.* J. Fluid Mech., vol. 570, pp. 347–364(2007).

[25] Ringuette, M. Wu, M., Martín, M. P. *Low Reynolds Number Effects in a Mach 3 Shock/Turbulent-Boundary-Layer Interaction.* AIAA J., Vol. 46, No. 7, pp.1884-1887(2008).

[26] Wu, M., Martín, M. P. *Analysis of Shock Motion in Shockwave and Turbulent Boundary Layer Interaction Using Direct Numerical Simulation Data.* J. Fluid Mech., Vol. 594, pp. 71–83(2008).

[27] Ringuette, M. J. Wu, M., Martín, M. P. *Coherent Structures in Direct Numerical Simulation of Turbulent Boundary Layers at Mach 3*. J. Fluid Mech., vol. 594, pp. 59–69(2008).

[28] Priebe, S. Wu, M., Martín, M. P. *Direct Numerical Simulation of a Reflected-Shock-Wave/Turbulent-Boundary-Layer Interaction.* AIAA J., Vol. 47, No. 5, pp.1173-1185(2009).

[29] Bookey, P. Wyckham, C., Smits, A. *Experimental Investigations of Mach 3 Shock-Wave Turbulent Boundary Layer Interactions.* AIAA Paper 2*005-4899*, 2005.

[30] LCattafesta III, L.N, Sheplak, M., *Actuators for active flow control*, Annual Review of Fluid Mechanics 43 (2011) 247–272. doi:10.1146/annurev-fluid-122109-160634.

[31] Blinde, P.L., Humble, R. A., van Oudheusden, B.W., Scarano, F., *Effects of micro-ramps on a shock wave/turbulent boundary layer interaction.* Shock Waves 19 (6) (2009) 507–520. doi:10.1007/s00193-009-0231-9.

[32] Saad, R., Erdem, E., Yang, L., Kontis, K., *Experimental studies on micro ramps at Mach 5*, in: Paper 2816, Proceedings of the 28th International, Symposium on Shock Waves, Manchester, U.K., 17–22 July, 2011.

[33] Sun, Z., Schrijer, F.J.J., van Oudheusden, F.S.B.W., *The three dimensional flow organization past a micro-ramp in a supersonic boundary layer*, in press, Physics of Fluids (2012).

[34] Ko¨nig, B., Pa¨tzold, M., Lutz, T., Kra¨mer, E., Rosemann, H., Richter, K., Uhlemann, H., *Numerical and experimental validation of three dimensional shock control bumps*, Journal of Aircraft 46 (2) (2009) 675–682. doi:10.2514/1.41441.

[35] Marxen, O., Rist, U., *Mean Flow Deformation in a Laminar Separation Bubble: Separation and Stability Characteristics*, Journal of Fluid Mechanics (2010), vol. 660, pp. 37-54.

[36] Smits, A. J., Dussauge, J. P. *Turbulent Shear Layers in Supersonic Flow*, 2nd ed., Springer Verlag, New York(2006).

[37] Boris, J. P. Grinstein, F. F.,. Oran, E. S , Kolbe, R. J. *New insights into large eddy simulation*. J. Fluid Dyn. Res., Vol. 10, 1992, pp. 199-228.

[38] Fureby C. , Grinstein, F. F. *Monotonically Integrated Large Eddy Simulation of Free Shear Flows.* AIAA J., Vol. 37, No. 5, pp.544-556(1999).

[39] Fureby C., Grinstein, F. F. *Large Eddy Simulation of High-Reynolds-Number and wall-Bounded Flows.* J. Comput. Phys., Vol. 181, pp. 68-97(2002).

[40] Grinstein, F. F., Margolin, L. G., Rider, W. J. *Implicit Large Eddy Simulation*, Cambridge university press(2007).

[41] Visbal, M. R., Morgan, P. E. , Rizzetta, D. P. *An Implicit LES Approach Based on High-Order Compact Differencing and Filtering Scheme.* AIAA paper 2003-4098.

[42] Morgan, P. E. Rizzetta D. P. , Visbal, M. R. *Large-Eddy Simulation of Separation Control for Flow over a Wall-Mounted Hump.* AIAA J., Vol. 45, No. 11, pp.2643-2660(2007).

[43] Rizzetta, D. P. Visbal, M. R. Gaitonde, D. *Large-Eddy Simulation of the Supersonic Compression-Ramp Flow by High-Order Method.* AIAA J., Vol. 39, No. 12,(2001).

[44] Rizzetta, D. P. Visbal, M. R. *Application of Large-Eddy Simulation to Supersonic Compression Ramps.* AIAA J., Vol. 40, No.8, pp.1574-1581(2002).

[45] Garnier, E. *On the Use of Shock-Capturing Schemes for Large-Eddy Simulation.* J. Comput. Phys., Vol. 153, pp. 272-311(1999).

[46] Ladeinde, F. Cai, X. , Visbal, M. R. , Gaitonde, D. V. *Turbulent spectra characteristics of high order schemes for direct and large eddy simulation*. Applied Num. Math., Vol. 36, pp. 447-474(2001).

[47] Gao, R. Yu, J, Kong, W., Yan, C. *Evaluation of a WENO Method in Implicit Large Eddy Simulation of Circular Cylinder Flow.* The 2nd International Conference on Computer and Automation Engineering (ICCAE), Vol. 5(2010).

[48] G.S. Jiang and C.W. Shu, *Efficient implementation of weighted ENO scheme*. J. Comput. Phys. 126 (1996), pp. 202–228.

[49] Cockburn, B., Shu, C. W. *TVD Runge-Kutta Local Projection Discontnuous Galerkin Finite Element Method for Conservation Laws II: General FrameWork.* Mathematics of Computation, Vol. 52, No. 186, pp.411-443(1989).

[50] Spekreijse, S. P. *Elliptic Grid Generation Based on Laplace Equations and Algebraic Transformations.* J. Comput. Phys., Vol. 118, pp.38-61(1995).

[51] Li, Q., Liu, C. *LES for Supersonic Ramp Control Flow Using MVG at M=2.5 and* Re_θ*=1440*. AIAA paper 2010-592.

[52] Lund, T. S., Wu, X., Squires, K. D. *Generation of turbulent inflow data for spatially developing boundary layer simulations.* J. Comput. Phys. 140, 233–258(1998).

[53] Liu C. and Chen, L. *Study of Mechanism of Ring-Like Vortex Formation in Late Flow Transition.* AIAA Paper 2010-1456.

[54] Guarini, S. E.; Moser, R. D.; Shariff, K; Wray, A. *Direct numerical simulation of a supersonic turbulent boundary layer at Mach 2.5*. Journal of Fluid Mechanics, vol. 414, Issue 01, p.1-33(2000)

[55] Tufo, H. M. , Fischer, P. F., Papka, M. E. , Blom, K. *Numerical Simulation and Immersive Visualization of Hairpin Vortices.* Conference on High Performance Networking and Computing archive, Proceedings of the 1999 ACM/IEEE conference on Supercomputing (CDROM) (1999).

[56] Lu, F. Liu, C. Li, Q, Pierce, A. *Experimental and Numerical Study of Multi-Ring Mechanism from Micro Vortex Generators for Shock/Boundary Layer Interaction Control.* AIAA paper 2010–4623.

[57] Li, Q., Yan, Y. Liu, C. Lu F., Pierce, A. *Numerical and experimental studies on the separation topology of the MVG controlled flow at M=2.5 and* Re_θ*=1440*. 49th AIAA Aerospace Sciences Meeting(2011).

[58] Manisankar,C., Verma, S.B., and Raju, C., *Shock-Wave Boundary-Layer Interaction Control on a Compression Corner Using Mechanical Vortex Generators*. 28th International Symposium on Shock Waves, Manchester, UK, July 17-22 2011, Paper-2446.

[59] Sun, Z., Schrijer, F.F.J., Scarano, F., and Oudheusden, B.W.V., "PIV Investigation of the 3D Instantaneous Flow Organization behind a Micro-Ramp in a Supersonic Boundary Layer, " University of Delft, ISSW28, July 17-22, 2011, Manchester, UK

[60] D. S. Dosanjh and T. M. Weeks, “Interaction of a starting vortex as well as a vortex street with a traveling shock wave,” AIAA J., Vol. 3, 1965, pp. 216-223.

[61] O. Inoue and Y. Hattori, “Sound generation by shock-vortex interactions,” J. Fluid Mech., Vol. 380, 1999, pp. 81-116.

[62] F. Grasso and S. Pirozzoli, “Shock-Wave-Vortex Interactions: Shock and Vortex Deformation and Sound Production,” Theoret. Comput. Fluid Dynamics, Vol. 13, 2000, pp.421-456.

BIOGRAPHICAL INFORMATION

Yonghua Yan has received a Bachelor of Science degree in Theoretical and Applied Mechanics and a Master degree in Fluid Mechanics from Shanghai University in China. His research at the University of Texas at Arlington has earned his a Department of Mathematics Outstanding Graduate Research Award in 2012. His research interests include the numerical simulation of Navier-Stokes flows.